PLASMA DYNAMICS

X. PLASMA PHYSICS*

Prof. S. C. Brown
Prof. G. Bekefi
Prof. K. U. Ingard
Prof. D. R. Whitehouse
Dr. J. C. Ingraham
M. L. Andrews
V. Arunasalam
C. D. Buntschuh
F. X. Crist
J. K. Domen
E. W. Fitzgerald, Jr.
D. L. Flannery
G. A. Garosi
W. H. Glenn, Jr.
E. B. Hooper, Jr.
P. W. Jameson
R. L. Kronquist
J. J. Linehan
D. T. Llewellyn-Jones
E. M. Mattison
J. J. McCarthy
W. J. Mulligan
J. J. Nolan, Jr.
G. L. Rogoff
F. Y-F. Tse
B. L. Wright

A. ION-CYCLOTRON OSCILLATIONS IN A PLASMA

1. Hollow-Cathode Arc

A hollow-cathode arc plasma source[1] has been constructed for use in the ion-cyclotron resonance experiment. The arc is shown schematically in Fig. X-1.

The vacuum chamber proper is constructed of commerical Pyrex pipe, with neoprene O-rings providing a seal between adjacent sections. The I.D. of the chamber in the plasma region is 2 inches. The bellows section is inserted to give some flexibility in the final alignment of the system. The water-cooled copper section near the cathode may be used as an anode in the reflex mode of operation of the arc.

The cathode and anode assemblies are supported by 5/8 inch stainless-steel tubes that pass through sliding seals at the ends of the system. The cathode itself is a 1/8 inch diameter, 0.010-inch wall tantalum tube that is press-fitted into a stainless-steel plug in the end of the cathode support. A cathode length of 4 inches or more eliminates the need for water-cooling of the cathode support. The anode is a 1.5-inch diameter disc of stainless steel or copper and is water-cooled.

The vacuum chamber is pumped at each end by a 6-inch oil diffusion pump with an unbaffled speed of 1500 liters per second. These pumps are backed by a single 40 c.f.m. mechanical pump. With the liquid-nitrogen-cooled baffles and the 6-inch gate valves, a total useful pumping speed of approximately 1200 liters per second is realized. The gate valves are of the continuously adjustable type so that the pumping speed at each end of the system may be varied from zero to the maximum of 600 liters per second. This facility has been found useful in stabilizing the arc in some modes of operation. The ultimate vacuum obtainable with the present system is $\sim 2 \times 10^{-7}$ mm Hg. The gas load contributed by the sliding seals and the O-rings is believed to be the factor limiting the ultimate pressure.

The pressure in the system is monitored by a thermocouple gauge and a Bayard-Alpert ionization gauge at each end of the system. A mercury MacLeod gauge, isolated

*This work was supported in part by the U.S. Atomic Energy Commission (Contract AT(30-1)-1842).

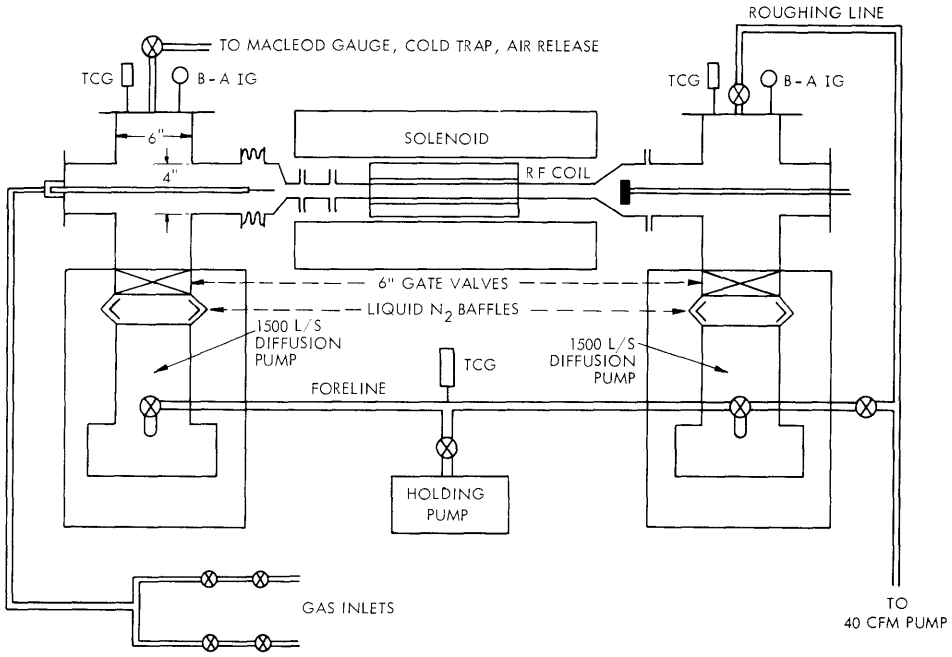

Fig. X-1. Schematic representation of the hollow-cathode arc.

from the system by a bellows valve and a cold trap, allows the absolute calibration of these gauges for each gas to be used.

The gas inlet to the cathode is controlled by two needle valves connected in series with two bellows valves, thereby allowing the admission of an arbitrary mixture of two gases into the system. The gas-flow rates are monitored individually by float-type flowmeters.

The confining magnetic field for the arc is produced by a solenoid, 80 cm in length with a 17-cm I.D., consisting of 13 equally spaced coils separated by cooling sections. A maximum continuous field of 4100 gauss may be achieved with a power dissipation of 20 kw. A partial flux return is provided by two end plates made of 3/8 inch thick hard-rolled steel having an aperture equal to the solenoid I.D. The solenoid is electrically compensated to produce a field inhomogeneity of less than 0.3 per cent within a cylinder, 4 cm in diameter and 40 cm long, centered in the solenoid.

The arc is started with a commercial welding starter and is run with a regulated DC power supply. It has been run in argon and helium and mixtures thereof, and its operating characteristics are generally similar to those reported by Lidsky and others.[1]

2. Ion-Cyclotron Resonance Experiment

The interaction of a magnetically confined plasma with a radiofrequency field near the ion-cyclotron frequency is of considerable interest both as a method for ionic heating

in thermonuclear devices[2] and as a diagnostic tool for laboratory plasmas. An experiment directed toward the latter end is now in progress. From measurements of the location and line shape of the ion-cyclotron resonance peak, it is possible, in principle, to determine ionic densities and temperatures and to obtain information on ionic collision cross sections.

The experiment is best understood in reference to the apparatus shown in Fig. X-1 and in detail in Fig. X-2. The plasma column of the hollow-cathode arc passes through the central region of the RF coil. There in addition to the static magnetic field B_o it is subjected to a time-variant magnetic field B_1 given, to first order, by

$$B_1 = B_1^o \sin \omega t \sin kz, \qquad |z| < L/2$$

$$= 0, \qquad |z| > L/2$$

where $L = 30$ cm, $\omega = 2\pi \times 10^6$, $k = \pi \times 10^{-1}$ cm^{-1}, and

$$B_o \cong \frac{m_i \omega}{2\pi Z_i e}, \qquad (\omega_{ci} \cong \omega).$$

The shield between the RF coil and the plasma serves to screen out the conservative, axially directed electric field associated with the coil so that the only electric field seen by the plasma is the solenoidal one arising from $\partial B_1/\partial t$. Physically, this shield is a glass tube that is coated with a layer of conducting paint having a resistivity of approximately 100 ohms per square. As the thickness of this layer is much less than the RF skin depth, the magnetic field can penetrate virtually unattenuated while the conservative electric field is effectively short-circuited.

Within the RF coil, then, there is an electric field given by

$$E_\theta^o = \frac{1}{2} \omega B_1^o r \cos \omega t \sin kz.$$

This field interacts with the plasma ions and sets up a current distribution in the plasma. The resultant magnetic field induces an electric field E_θ^1 which, back at the RF coil, is evidenced by a change in impedance

$$\frac{\Delta z}{z_o} = \frac{\left\langle E_\theta^{1*} \cdot J \right\rangle_{av}}{\left\langle E_\theta^{o*} \cdot J \right\rangle_{av}},$$

where the average is taken over the windings of the coil.

J = current distribution in the RF coil

$$\Delta z = \Delta R + \Delta LS \sim \mathrm{Re} \left\langle E_\theta'^{*} \cdot J \right\rangle + i\, \mathrm{Im} \left\langle E_\theta'^{*} \cdot J \right\rangle .$$

The coil itself is the unknown element in a sensitive RF bridge, which has been described previously in detail.[3] The magnetic field is modulated at 100 cps by the

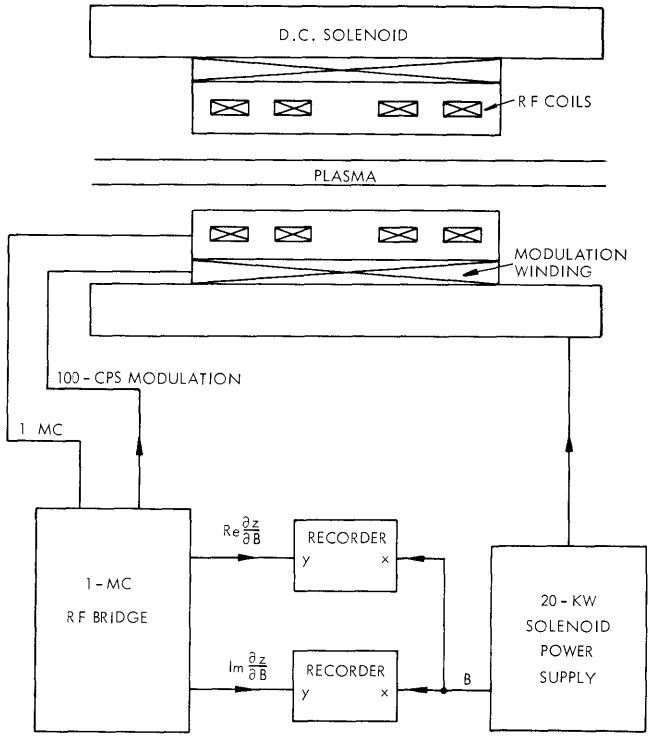

Fig. X-2. Ion-cyclotron resonance system.

additional winding shown in Fig. X-2. An unbalance signal at $\omega = 2\pi(10^6+10^2)$ with a complex amplitude proportional to

$$\frac{d\,\Delta z}{d\,B}$$

is thus produced. This signal is amplified and heterodyned to 100 cps, and then synchronously detected with reference to the modulation signal. Thus at the output of the bridge, two DC signals proportional to Re d/dB Δz and Im d/dB Δz are available. These are plotted as the ordinates on a pair of x-y recorders, the common abscissa being a signal proportional to the DC magnetic field. If the DC field is then slowly scanned, the derivatives of the absorption and dispersion spectra are displayed.

If we assume a cold, constant collision-frequency model for the plasma ions, it can be shown that for low densities ($\epsilon<1$)

$$\Delta z \sim \frac{i\epsilon(1+i\gamma)[\beta^2-\epsilon(1+i\gamma)]}{\beta^2[\beta^2-(1+i\gamma)(1+\epsilon+i\gamma)]}$$

$$\beta = \frac{\omega_{ci}}{\omega} = Z_i \frac{eB_o}{m_i\omega}$$

$$\gamma = \frac{\nu_{ci}}{\omega}$$

$$\epsilon = \frac{\omega_{pi}^2}{k^2c^2}.$$

That is, an essentially Lorentzian resonant absorption will occur when $\beta^2 = 1 + \epsilon - \gamma^2$ with a width determined by γ and a height proportional to ϵ/γ. Thus the density and dominant cross section for ion energy loss may be determined from a measurement of the absorption line.

In the arc plasma the ions will have a thermal spread in velocity. In passing through the RF coil, an ion with an axial velocity v_z will not be resonant at $\omega = \omega_{ci}$, but rather at $\omega = \omega_{ci} \pm kv_z$. The thermal spread will average over these shifted resonances and will produce a Gaussian absorption line with a width determined by kv_T/ω.

The relative importance of these two broadening mechanisms is determined by the relative magnitudes of γ and kv_T/ω. The space periodicity of the coil $\lambda = 2\pi/k$ may be chosen so that either one of the two mechanisms is dominant. For example, in a helium plasma with $T_i \cong 1$ ev and a neutral background pressure of 5×10^{-3} torr:

λ	k	kv_T/ω	γ^*	
20 cm	$\pi \times 10^{-1}$	0.05	0.12	collision broadened
2 cm	π	0.5	0.12	transit-time broadened

*estimated neutral elastic and charge transfer cross section.[4]

The apparatus described in this report is now fully operational. Data are being taken in helium and helium-argon in the collision-broadened region. Hydrogen and hydrogen-helium plasmas will also be investigated and absorption in the transit-time-broadened region will be studied.

W. H. Glenn, Jr.

References

1. L. M. Lidsky, S. D. Rothleder, D. J. Rose, and S. Yoshikawa, J. Appl. Phys. 33, 2490 (1962).

2. T. Stix, Phys. Fluids 1, 308 (1958).

3. J. W. Graham and R. S. Badessa, Quarterly Progress Report, Research Laboratory of Electronics, M.I.T., April 15, 1958, pp. 7-11.

4. S. C. Brown, Basic Data of Plasma Physics (The Technology Press of Massachusetts Institute of Technology, Cambridge, Mass., and John Wiley and Sons, Inc., New York, 1959).

B. FRAUNHOFER ANALYSIS OF DIFFRACTION GRATINGS FOR THE FAR INFRARED

Although there is nothing new about the Fraunhofer analysis of diffraction gratings, it has often been found that in nearly symmetric small blaze angle gratings, or when the grating spacing is only a few times larger than the wavelength, that important terms are not properly evaluated.[1] A clear outline of the Fraunhofer analysis has been given by Rowland.[2] It consists of considering each ray incident on the grating as radiating a spherical wave from the surface of the grating whose phase is determined by path length relative to some reference ray in the incident beam. Then the amplitudes, with phases of all rays in these spherical waves parallel to some chosen spacial direction, are summed to give the Fraunhofer intensity from the grating in that direction, which is obtained physcially by observing at the focal point of a condensing lens, or at a distance far away compared with the grating size. Expressed mathematically,

$$U_{\vec{r}} = \int_S u_{\vec{r}}(s)\, e^{-i\phi(s)}\, dS,$$

where $u_{\vec{r}}(s)$ is the amplitude of the ray coming from the point s on the surface of the grating in the direction $\vec{r}$, and $\phi(s)$ is the phase of this ray relative to the reference ray both taken at the point of observation. Note that the surface S may be the surface of the grating, but can be any surface with a one-to-one correspondence with the grating surface. Then the intensity at the point of observation is $I_{\vec{r}} = U^*_{\vec{r}} U_{\vec{r}}$.

Let us consider a blazed reflection grating (Fig. X-3), with a plane wave with constant intensity wave front incident upon the grating at angle ψ in the (x, y) plane. We shall assume that the grating groove (z-direction) is very long compared with a wavelength, so that only the diffraction in the (x, y) plane need be considered. The problem then reduces to a line integral that for Fig. X-3 is

$$U_\theta = u\left\{\sum_{k=0}^{N-1} e^{-i\phi_{OB^k}} \int_0^{a_1} e^{-i\phi_{OA}\frac{y}{a_1}}\, dy + \sum_{k=0}^{N-1} e^{-i[\phi_{OA}+\phi_{OB^k}]} \int_0^{a_2} e^{-i\phi_{AB}\frac{y}{a_2}}\, dy\right\},$$

where u is the ray amplitude (in this case independent of θ and y because the intensity

of incident radiation falling on dy is independent of y), and ϕ_{12} is the phase of point 1 relative to the origin minus the phase of point 2 relative to the origin. For convenience,

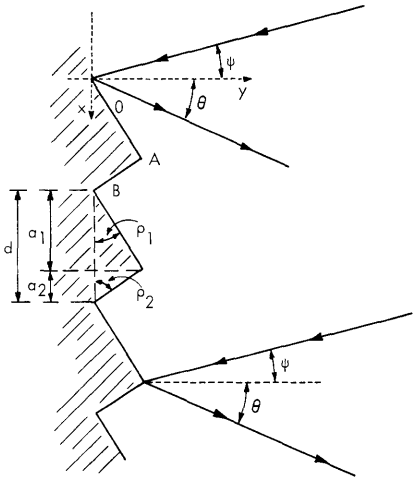

Fig. X-3. Blazed reflecting grating.

the phase at the origin has been called zero, that is, the phase difference from the origin to the point of observation has been subtracted from everything, since only relative phase is of importance. The rest of the symbols, except for N, the total number of grooves in the grating, are defined by Fig. X-3.

Integrating U_θ out and multiplying by its complex conjugate, for the intensity we have

$$I_\theta = u^2\left(\frac{\sin N\alpha}{\sin \alpha}\right)^2 \left\{\left(a_1 \frac{\sin \beta}{\beta}\right)^2 + \left(a_2 \frac{\sin \gamma}{\gamma}\right)^2 + 2a_1a_2 \frac{\sin \beta}{\beta} \frac{\sin \gamma}{\gamma} \cos (\beta+\gamma)\right\},$$

where

$$\alpha = \frac{1}{2}\phi_{OB} = \frac{\pi d}{\lambda} [\sin \psi - \sin \theta]$$

$$\beta = \frac{1}{2}\phi_{OA} = -\frac{\pi a_1}{\lambda \cos \rho_1} [\sin (\rho_1+\theta) + \sin (\rho_1-\psi)]$$

$$\gamma = \frac{1}{2}\phi_{AB} = \frac{\pi a_2}{\lambda \cos \rho_2} [\sin (\rho_2-\theta) + \sin (\rho_2+\psi)]$$

so that

$$\alpha = \beta + \gamma.$$

It is just this cross term of the diffraction envelopes for a_1 and a_2, the third term in

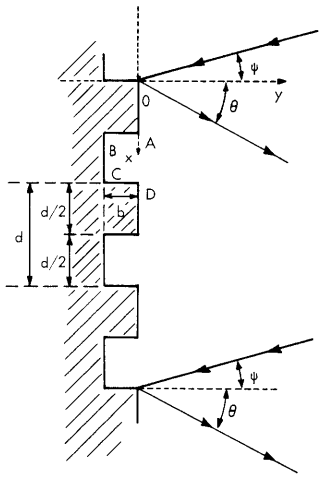

Fig. X-4. Lamellar reflection grating.

I_θ, which can make an important contribution to the intensity when a_1 and a_2 are nearly equal and d/λ is not too large.

If this grating were instead a transmission grating with an index of refraction n and a plane back surface in the (x, z) plane with the incident radiation making an angle ψ with the negative y axis, then the same equation would hold for I_θ. Now,

$$\alpha = \frac{1}{2}\phi_{OB} = \frac{\pi d}{\lambda}\left[\sin\psi - \sin\theta\right]$$

$$\beta = \frac{1}{2}\phi_{OA} = -\frac{\pi a_1}{\lambda\cos\rho_1}\left[\sin(\rho_1+\theta) - n\sin(\rho_1+\psi')\right]$$

$$\gamma = \frac{1}{2}\phi_{AB} = \frac{\pi a_2}{\lambda\cos\rho_2}\left[\sin(\rho_2-\theta) - n\sin(\rho_2-\psi')\right]$$

and

$$\sin(\psi') = \frac{1}{n}\sin(\psi).$$

Again,

$$\alpha = \beta + \gamma.$$

Another grating that has been of interest for the far infrared is the lamellar reflection grating illustrated in Fig. X-4. In this case,

$$U_\theta = u\left\{\sum_{k=0}^{N-1} e^{-i\phi_{OD}k}\int_0^{d/2} e^{-i\phi_{OA}}\frac{y}{d/2}\,dy + \sum_{k=0}^{N-1} e^{-i(\phi_{OB}+\phi_{OD}k)}\int_0^{d/2} e^{-i\phi_{BC}}\frac{y}{d/2}\,dy\right\},$$

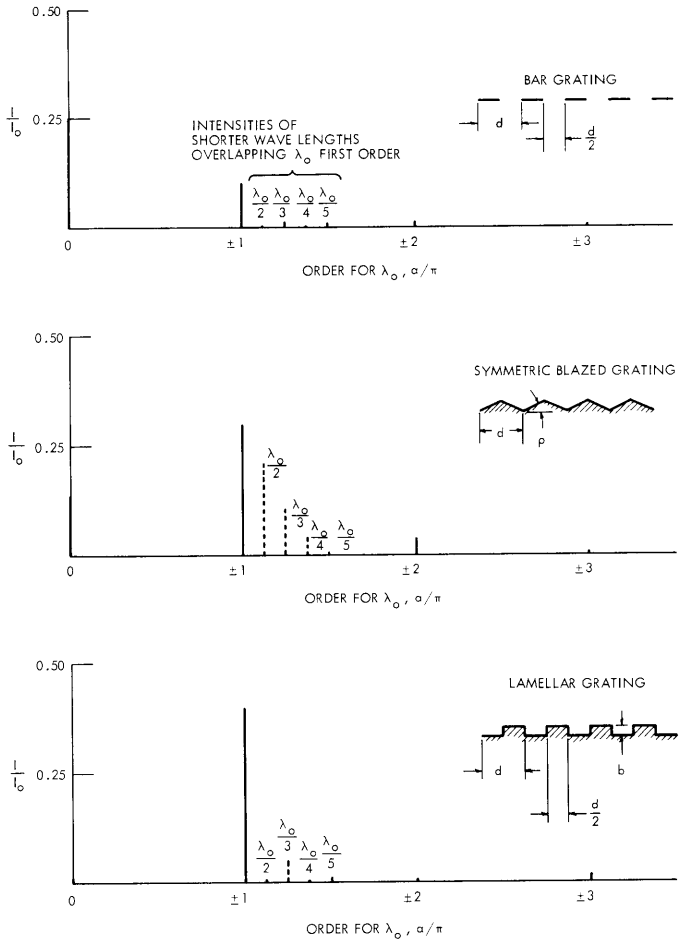

Fig. X-5. Comparison of reflection gratings. (I/I_o maximized for symmetric first order.)

in which any shadow effect in the valleys has been neglected. We obtain

$$I_\theta = u^2\left(\frac{\sin N\alpha}{\sin \alpha}\right)^2 \left(d\,\frac{\sin \alpha/2}{\alpha/2}\right)^2 \cos^2(\alpha/2+\beta/2),$$

where

$$\alpha = \frac{1}{2}\phi_{OD} = \frac{\pi d}{\lambda}[\sin\psi - \sin\theta]$$

$$\beta = \phi_{AB} = \frac{2\pi b}{\lambda}[\cos\psi + \cos\theta].$$

This is to be contrasted with an ordinary bar grating in which all recessed flats like BC are perfectly absorbing. Then,

$$I_\theta = u^2 \left(\frac{\sin N\alpha}{\sin \alpha}\right)^2 \left(d/2 \, \frac{\sin \alpha/2}{\alpha/2}\right)^2 .$$

If one is interested in producing in the far infrared a beam splitter that gives two identical beams with the greatest intensity and of narrow bandwidth, a symmetric reflection grating would seem to be the easiest thing. The equation for the symmetric blazed reflection grating, $\rho_1 = \rho_2 = \rho$ and $a_1 = a_2 = \frac{d}{2}$, is

$$I_\theta = u^2 \left(\frac{\sin N\alpha}{\sin \alpha}\right)^2 \left(\frac{d}{2}\right)^2 \left\{\left(\frac{\sin \beta}{\beta}\right)^2 + \left(\frac{\sin \gamma}{\gamma}\right)^2 + 2 \, \frac{\sin \beta}{\beta} \, \frac{\sin \gamma}{\gamma} \cos \alpha\right\}.$$

Here, with $\psi = 0$ to take advantage of the symmetry, we have

$$\alpha = - \frac{\pi d}{\lambda} \sin \theta$$

$$\beta = - \frac{\pi d}{2\lambda \cos \rho} \left[\sin (\rho+\theta) + \sin \rho\right]$$

$$\gamma = \frac{\pi d}{2\lambda \cos \rho} \left[\sin (\rho-\theta) + \sin \rho\right].$$

In Fig. X-5 we compare the bar, symmetric-blazed, and lamellar reflection gratings when given a specific beam angle, $\theta_o = 18°$. The efficiency of the gratings has been maximized for the first-order λ_o corresponding to this beam angle; $\lambda_o = d \sin \theta_o$, where d, of course, determines λ_o but the normalized intensities are independent of the ratio d/λ_o. For the intensity normalization we have taken $I_o = (uNd)^2$. Optimizing the efficiency at $\theta_o = 18°$ gives $\rho = 12° 14'$ for the symmetric blazed grating, with $b/d = 0.1625$ for the lamellar grating. The solid lines in Fig. X-5 show the distribution of the intensity of λ_o radiation in its different orders, while the dotted lines give the intensities of frequency multiples $\lambda_o/2$ through $\lambda_o/5$ (with u assumed the same for each) which fall at the same angle θ_o and are, therefore, in the beam. It seems evident from this comparison that the lamellar grating makes the best small-angle beam splitter.

M. L. Andrews

References

1. R. F. Stamm and J. J. Whalen, Energy distribution of diffraction gratings as a function of groove form, J. Opt. Soc. Am. 36, 2-12 (1946).

2. H. A. Rowland, Gratings in theory and practice, Astron. and Astrophys. 12, 129-149 (1893).

C. PROBE STUDIES OF THE CENTRAL PLASMA COLUMN OF THE HOLLOW-CATHODE DISCHARGE

Langmuir-probe studies of the central plasma column of the hollow-cathode discharge system described by Buntschuh[1] have been conducted. Previous probe measurements by Starr[2] indicated plasma densities, N, greater than 10^{12} cm^{-3}, and electron temperatures, T_-, above 10 ev in the plasma surrounding the central column. The central plasma column was not entered during those studies, because of rapid heating and deterioration of the probes. A probe rotating at 1 cps on a radius of approximately ten times the plasma radius has enabled measurements in the central plasma, with little deterioration for arc currents, I_A, less than 20 amps. Plasma density and electron temperatures were obtained by using simple probe theory.

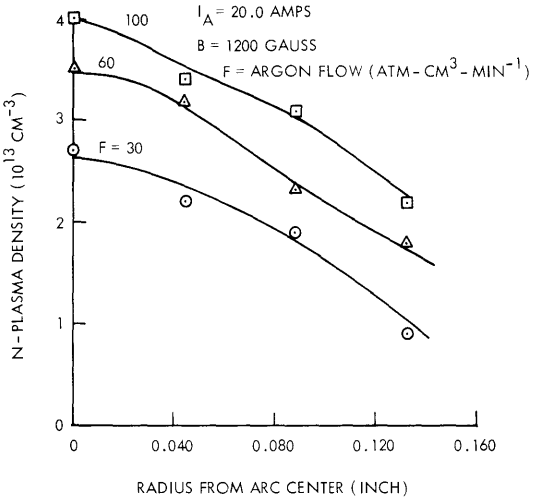

Fig. X-6. Variation of plasma density with radius for several flows (0.125-inch diameter cathode).

The probes were cylindrical surfaces on 0.015-inch diameter tungsten wire insulated with an aluminum-oxide coating. Probe areas were of the order of (5) 10^{-3} cm^2. The Debye length was much smaller than the probe radius, r_p, and all collision mean-free paths. The average Larmor radius was much greater than r_p for ions (argon), and of the same order as r_p for electrons. Thus planar probe theory is applicable to ion current and to electron current, provided that "drainage" perturbation is small. Electron temperature was calculated from the slope of log J_- versus voltage plots, and used to compute plasma density from ion saturation currents by

$$J_{+_s} = qN\left(\frac{qT_-}{m_+\epsilon}\right)^{1/2}, \tag{1}$$

where ϵ is the base of the natural logarithm. Equation 1 is the well-known result of presheath analysis for ion collection by a negative probe. Electron saturation currents were not generally collected, because of the probe heating which resulted, so plasma potential was only measured in a few cases.

The range of arc parameters was: argon flow, F; 30-100 atm-cm^3-min^{-1}, arc current, I_A; 10-20 amps, and magnetic field, B; 800-1200 gauss, with 0.125-inch

diameter tantalum cathodes. Limited data were taken with 0.250-inch and 0.375-inch diameter cathodes. Straight line log J_- versus voltage plots were obtained within a few per cent for all cases. The estimated accuracy of plasma density values is ± 15 per cent relative, and ± 50 per cent absolute.

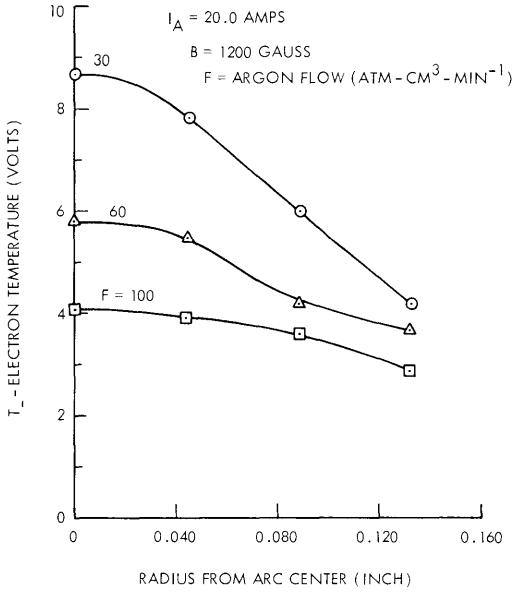

Fig. X-7. Variation of electron temperature with radius for several flows (0.125-inch diameter cathode).

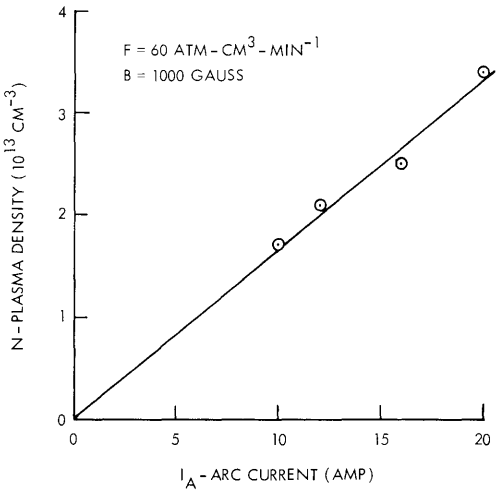

Fig. X-8. Plasma density at arc center vs arc current (0.125-inch diameter cathode).

The electron temperatures that were measured ranged from 3 ev to 9 ev, while the plasma density range was (1-4) 10^{13} cm^{-3}. Figures X-6 and X-7 illustrate the type of radial variation observed for N and T_-, and also variations with argon flow. Figure X-8 is a plot of N versus I_A showing apparent proportionality within the relative experimental accuracy. T_- increased slowly with arc current. Plasma density varied strongly with magnetic field, while electron temperature varied slowly. The measurements with larger cathodes show central-column densities above 10^{13} cm^{-3} and essentially uniform out to a radius equal to the cathode radius. These measurements were made with I_A = 15.0 amps, F = 120 atm-cm^3-min^{-1}, B = 1200 gauss. Electron temperature was approximately 3 ev for these conditions.

The few plasma-potential measurements that were made indicated that the central plasma potential was close to zero with respect to the anode, and a small positive radial gradient of a fraction of a volt per cm outside the central column existed. Densities above 10^{12} cm^{-3}, and electron temperatures of approximately 1 ev were measured in

stationary probe studies at radii up to 0.7 inch.

Further details and results of these studies may be found in the author's thesis.[3]

D. L. Flannery

References

1. C. D. Buntschuh, Hollow-cathode arc, Quarterly Progress Report No. 65, Research Laboratory of Electronics, M.I.T., April 15, 1962, pp. 79-87.

2. A. W. Starr, Probe Measurements in the Hollow Cathode Arc, S.M. Thesis, Department of Electrical Engineering, M.I.T., August 1961.

3. D. L. Flannery, Probe Studies of a Hollow Cathode Arc, S.M. Thesis, Department of Mechanical Engineering, M.I.T., May 1964.

D. USE OF INTERFEROMETRIC SPECTROSCOPY FOR FAR INFRARED PLASMA DIAGNOSTICS

Measurements of the real part of the complex refractive index of a plasma in the submillimeter region of the electromagnetic spectrum ($0.1\ \text{mm} < \lambda < 1.0\ \text{mm}$) have already been carried out[1] at $\lambda \approx 0.3$ mm with an interferometer that has severe limitations. These limitations arise because resolution is energy-limited (detector noise dominates the signal), whereas efficient functioning of the instrument is critically dependent upon the isolation of as narrow a bandwidth of radiation as possible. The reasons for this have been pointed out.[1]

If resolution is energy-limited, and the long integration times necessary to extract a signal from noise are undesirable, the technique of interferometric spectroscopy[2,3] has been shown[4] to be the most efficient far infrared spectroscopic method. This report summarizes its application to the study of the dielectric properties of plasmas.

1. Principle of Interferometric Spectroscopy

If radiation of a finite bandwidth is admitted to a Michelson interferometer, such as that shown in Fig. X-9, the component of the output intensity I which varies with path difference x between the two beams is given by

$$I(x) = \int_0^k \mathscr{I}(k) \cos(2\pi k x)\, dk, \tag{1}$$

where $\mathscr{I}(k)\, dk$ is the radiated power reaching the detector at wave numbers between k and $k + dk\ \text{cm}^{-1}$. $\mathscr{I}(k)$ is assumed to be nonzero only in the range $0 < k < K$.

Equation 1 can be regarded as the intensity profile of "white light" interference

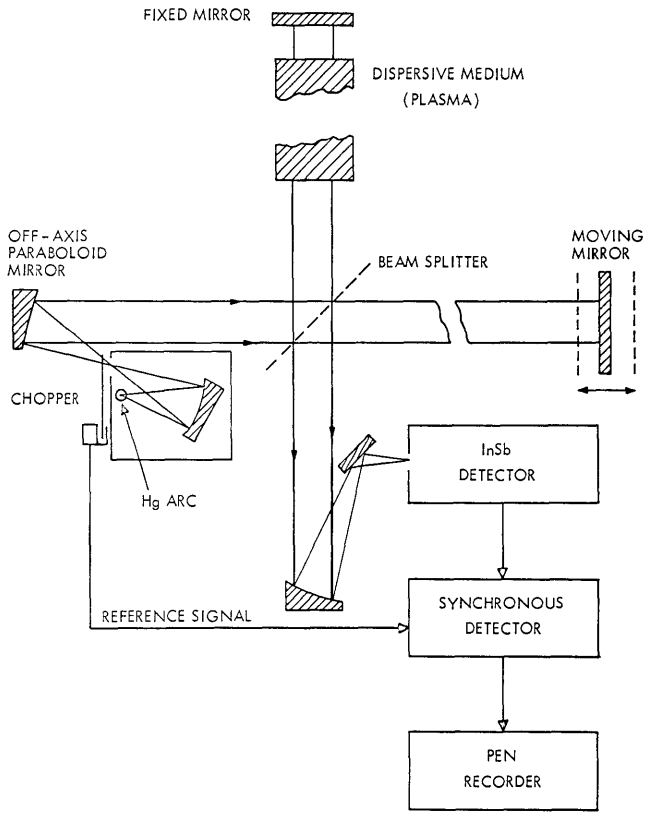

Fig. X-9. Far infrared Michelson interferometer for studying complex dielectric coefficients.

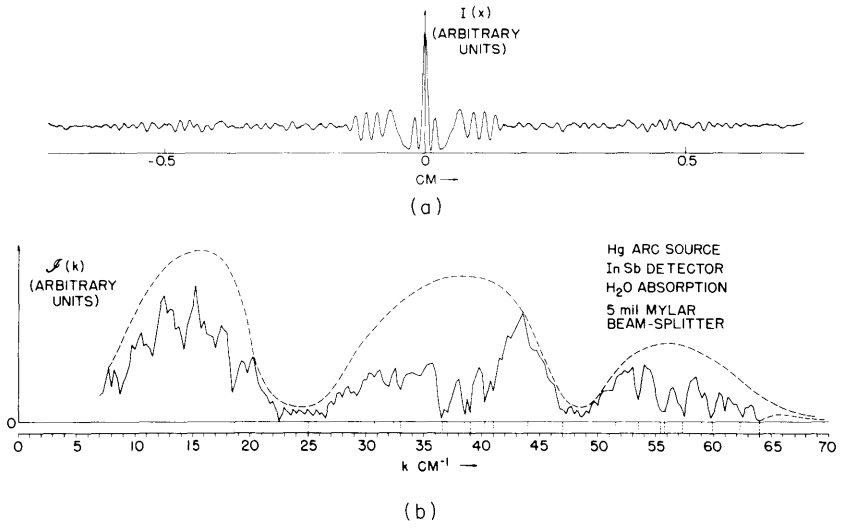

Fig. X-10. (a) Portion of typical interferogram. (b) Fourier transform of (a) showing water-vapor absorption and the beam-splitter efficiency (dotted envelope).

fringes. I(x) is known as an interferogram; an experimental example is shown in Fig. X-10a.

$\mathcal{I}(k)$ is clearly the cosine Fourier transform of I(x):

$$\mathcal{I}(k) = \int_{-\infty}^{+\infty} I(x) \cos (2\pi kx)\, dx. \tag{2}$$

I(x), however, is given experimentally only between definite limits, say $-X < x < X$. Thus it is possible, by numerical integration on a digital computer, to evaluate the function

$$\mathcal{I}'(k) = \int_{-X}^{+X} I(x) \cos (2\pi kx)\, dx. \tag{3}$$

Figure X-10b shows $\mathcal{I}'(k)$ evaluated from Fig. X-10a; the details of the spectrum are

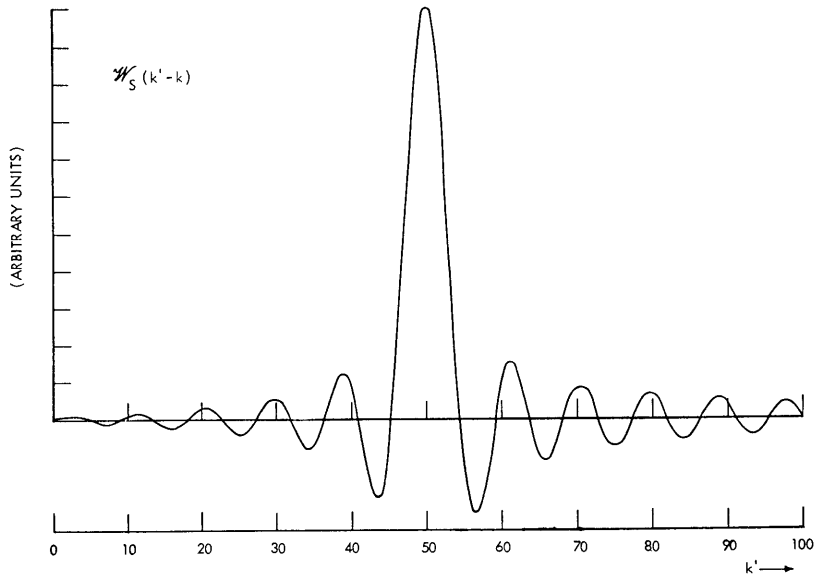

Fig. X-11. Unapodized scanning function for k = 50.

discussed in a later section. Equation 3 is the Fourier transform of I(x) weighted by a function W(x), which in Eq. 3 is a finite step function:

$$W_S(x) = \begin{cases} 1 & \text{for } -X < x < X \\ 0 & \text{elsewhere.} \end{cases}$$

From the convolution theorem[5]

$$\mathscr{I}'(k) = \int_{-\infty}^{+\infty} \mathscr{W}(k'-k)\ \mathscr{I}(k')\ dk', \tag{4}$$

which is the convolution of $\mathscr{I}(k)$ with a scanning function $\mathscr{W}(k'-k)$, where $\mathscr{W}(k)$ is the Fourier transform of W(x).

The scanning function is the instrumental line shape, that is, the interpretation, which this technique gives, of an infinitely narrow spectral line. This is verified by substituting $\mathscr{I}(k) = \delta(k_o-k)$ in Eq. 4. When W(x) is a finite step function, the scanning function is

$$\mathscr{W}_s(k'-k) = X\left\{\frac{\sin[2\pi(k'-k)X]}{[2\pi(k'-k)]} + \frac{\sin[2\pi(k'+k)X]}{[2\pi(k'+k)X]}\right\}. \tag{5}$$

The portion of this function for $k' > 0$ is illustrated in Fig. X-11. The influence of the term in (k'+k) is seen in the asymmetry of the function about $k' = k$. In practice, this influence is negligible and the second term will be neglected in the succeeding discussion.

2. Apodization

The scanning function Eq. 5 is an inconvenient one because of the large side lobes that will distort any high-resolution spectrum. They are the price that is paid for investigating the Fourier transform of a discontinuity (at $|x| = X$) in a wave train. Apodization

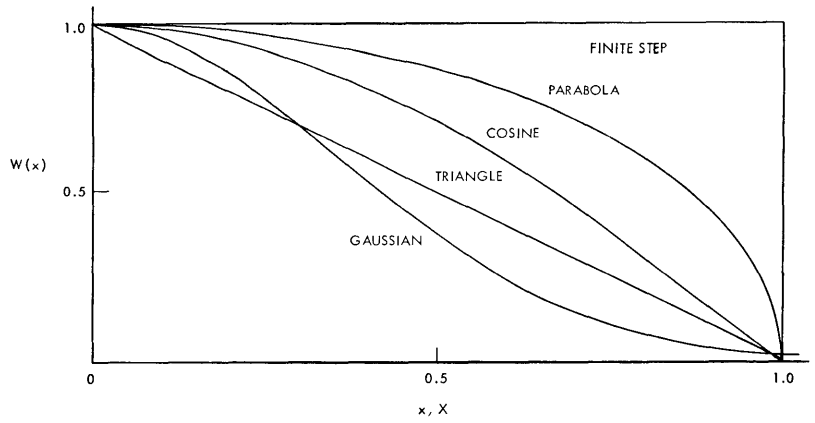

Fig. X-12. Four apodizing functions.

is a procedure of choosing a W(x) that does not exhibit a discontinuity, that is, which decreases monotonically to zero as $|x| \to X$. The simplest and most convenient such function is an isosceles triangle

$$W_T(x) = \begin{cases} 1 - \dfrac{|x|}{X}, & -X < x < X \\ 0 & \text{elsewhere,} \end{cases}$$

which gives the scanning function

$$\mathscr{W}_T(k'-k) = \frac{X}{2}\left\{\frac{\sin^2[\pi(k'-k)X]}{[\pi(k'-k)X]^2} + \ldots\right\}.$$

This function is the same as the instrumental linewidth of a diffraction grating when resolution is diffraction-limited (see Fig. X-13a).

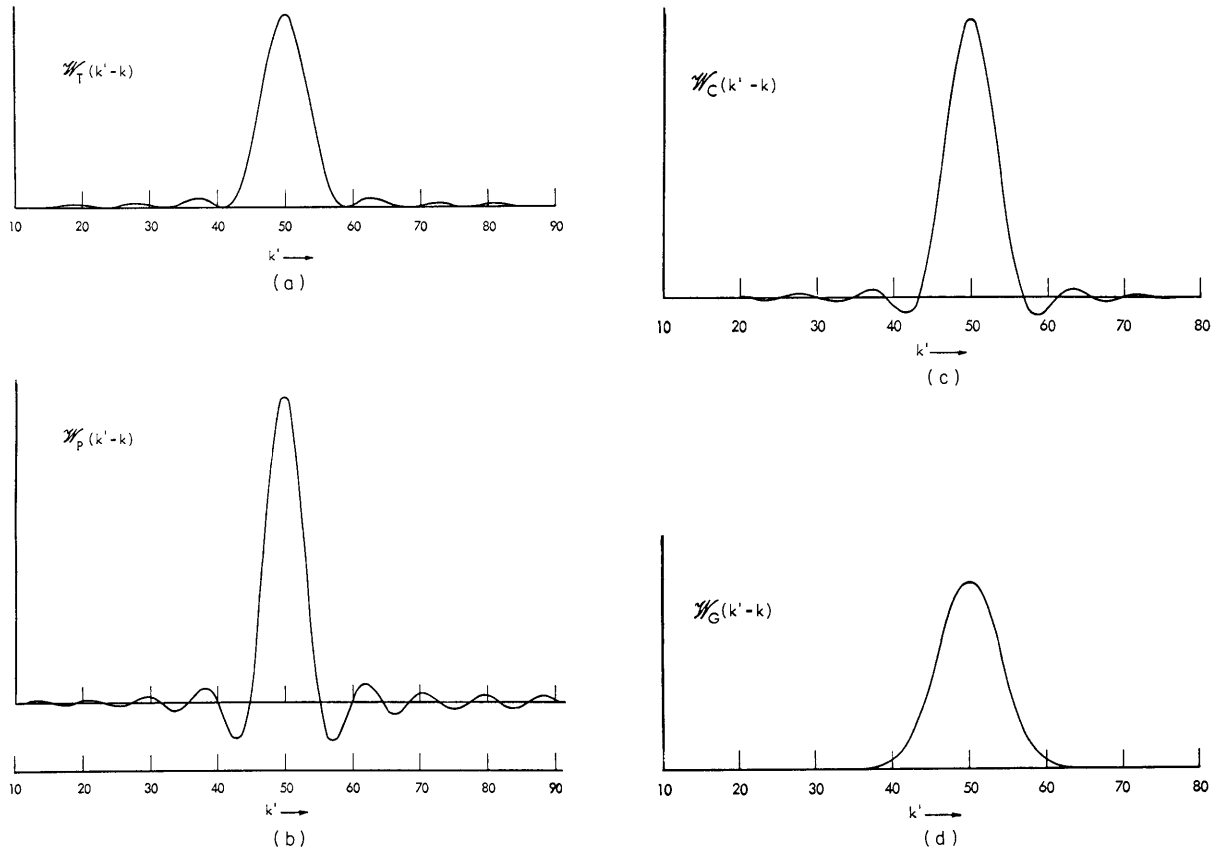

Fig. X-13. (a) Scanning function for triangular apodization. (b) Parabolic apodization. (c) Cosine apodization. (d) Gaussian apodization. (All figures to same scale as Fig. X-11.)

Four possible apodizing functions are shown together in Fig. X-12 and their transforms in Figs. X-13. Notice, qualitatively, how the width of the peak and the

suppression of the side lobes increase with the severity of the apodizing functions. The lobes are reduced only at the expense of resolution.

3. Resolving Power

Resolution is determined by the width of the peak of the scanning function. $\mathscr{W}_s(k'-k)$ goes to zero at $|k'-k| = 1/2X$, and $\Delta k = 1/2X$ may be conveniently be called the resolution width. For triangular apodization this width is doubled, but the line shape is also improved. The half-width of the line is increased by a factor of ~1.5.

4. Measurement of Complex Refractive Index

If a dispersive medium is placed in one of the beams, as indicated in Fig. X-9, the interferogram is given by

$$I(x) = \int_0^k a(k)\,\mathscr{I}(k)\,\cos\,[(2\pi kx)-\Phi(k)]\,dk,$$

where $\Phi(k)$ is a phase shift, and $a(k)$ is the square root of the transmission coefficient of the sample. They are related respectively to the real and imaginary parts of the refractive index of the sample.

$I(x)$ is expanded into its odd and even parts:

$$I(x) = \int_0^k \{A(k)\,\sin\,(2\pi kx)+B(k)\,\cos\,(2\pi kx)\}\,dk,$$

where

$$A(k) = a(k)\,\mathscr{I}(k)\,\sin\,[\Phi(k)],$$

$$B(k) = a(k)\,\mathscr{I}(k)\,\cos\,[\Phi(k)].$$

$$\therefore \quad \Phi(k) = \tan^{-1}\,[A(k)/B(k)]$$

and

$$a(k) = \sqrt{\frac{A^2(k) + B^2(k),\ \text{(sample in)}}{A^2(k) + B^2(k),\ \text{(sample out)}}},$$

while

$$\mathscr{I}(k) = \sqrt{A^2(k) + B^2(k),\ \text{(sample out)}}\ .$$

$A(k)$ and $B(k)$ are the sine and cosine Fourier transforms of $I(x)$, respectively. The sine transform of the cosine term in $I(x)$ must vanish (and vice versa) because the integrand is an odd function integrated between limits that are symmetrical about the origin.

All of these steps can be performed by digital computer.

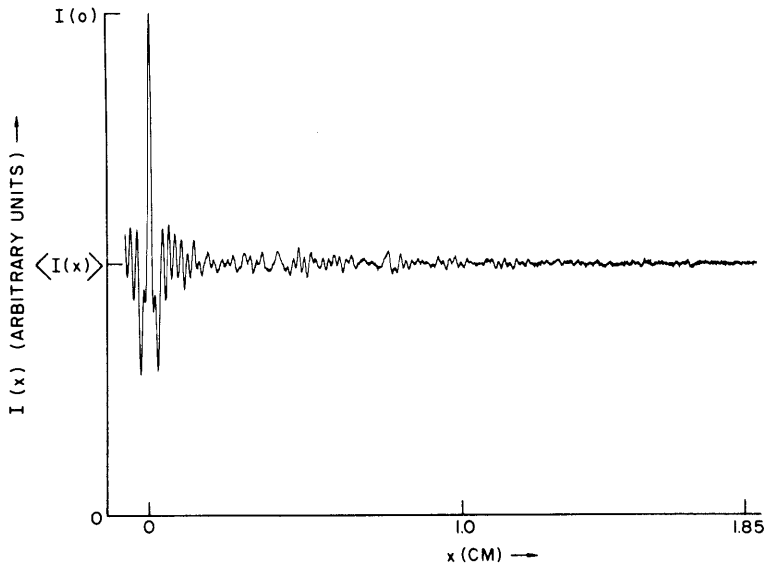

Fig. X-14. Half of interferogram used to compute Fig. X-15.

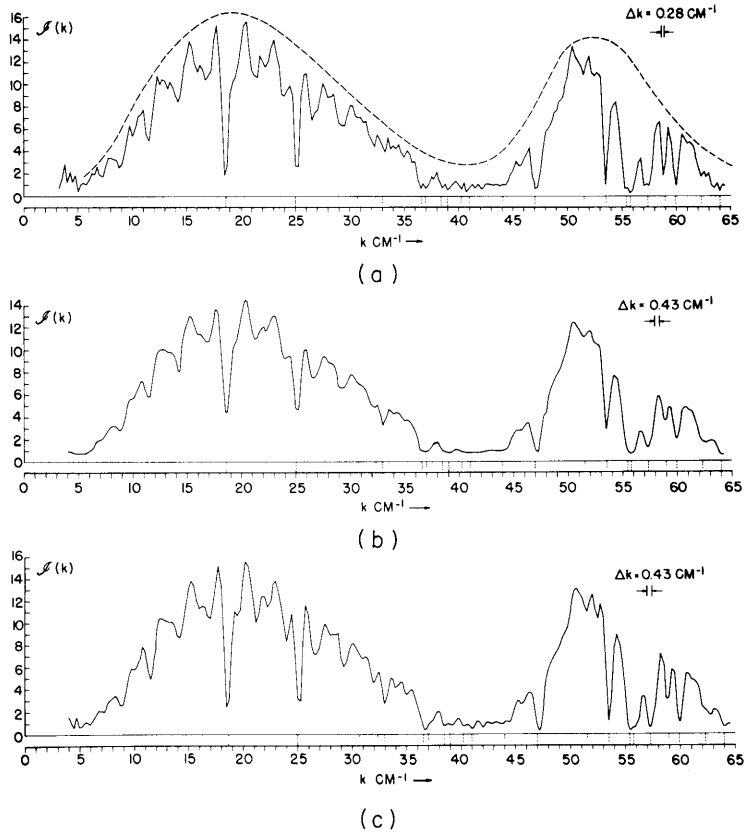

Fig. X-15. (a) Unadopized spectrum (from Fig. X-14). (b) Apodized spectrum. (c) Unadopized spectrum (resolution width increased by 1.5).

5. Results

The curves shown in Fig. X-13 were obtained by feeding 10 cycles of pure cosine to the computer program and have provided a useful test of the program's effectiveness.

Figure X-14 shows half of an interferogram obtained with the instrument shown schematically in Fig. X-9. Figure X-15 shows the spectrum unapodized, apodized with a triangle, and unapodized with the resolution width increased by 1.5.

The spectrum is modified by three factors:

(i) Characteristic of the beam splitter. Figure X-10 was obtained with a 5-mil mylar membrane beam splitter and Fig. X-15 with a 3-mil membrane. These give rise to a thin-film interference effect that is shown by the dotted envelopes.

(ii) Atmospheric water-vapor absorption. The positions and approximate strengths of known water-vapor absorption lines are shown on the k-axis (taken from authoritative measurements by Richards[6]). These lines distort the spectrum badly but provide a useful calibration of the instrument. Notice how the 0.29 cm^{-1} doublet at k = 55 cm^{-1} is just resolved in Fig. X-15a (as expected theoretically). Examination of Fig. X-15b and 15c indicates that the increase in resolution width, because of triangular apodization, is rather more than 1.5.

(iii) Thin film interference effect in the envelope of mercury arc source. Notice the dips separated by ~2.75 cm^{-1}, which are easily visible in the portion of the spectrum

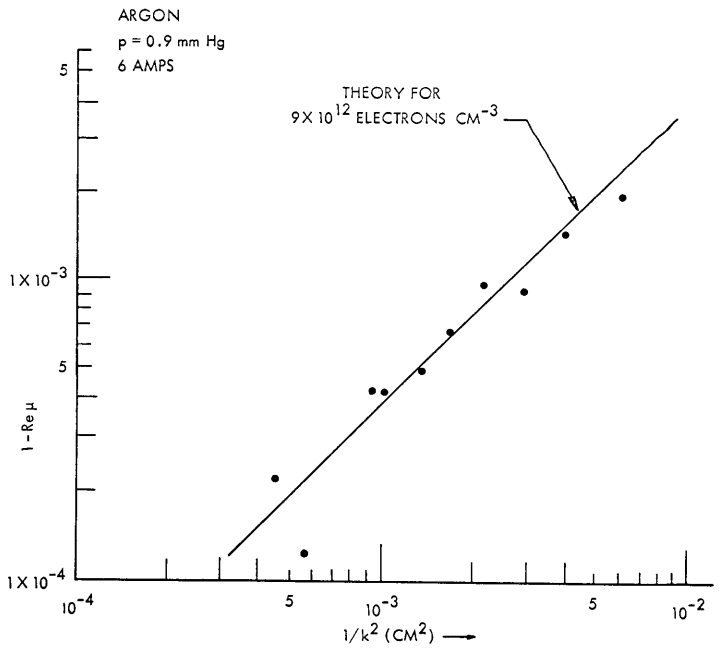

Fig. X-16. Far infrared measurements of the real part of the refractive index of a plasma.

for $k < 18$ cm^{-1} where no water vapor absorption is believed to occur. These can be removed by dimpling the fused-quartz envelope of the arc lamp.[6]

Figure X-16 shows measurements of the real part of the refractive index of a plasma. The points are fitted to an electron density of 9×10^{12} electrons cm^{-3}. The free-space infrared wavelengths that were used ranged between 0.22 mm and 0.72 mm.

6. Conclusion

This technique is desirable because resolution is energy-limited in this region of the spectrum. In contrast to a scanning spectrometer, the signal falling on the detector is at all times composed of all of the spectral components present. Thus it makes most efficient use of the detector. This technique has been used to measure the real part of the refractive index of a plasma, and the next step is to measure the imaginary part (absorption), too.

All computation work was done on the IBM 7094 computer at the Computation Center, M. I. T. This report is based on a Master's thesis submitted by the author to the Department of Physics, M. I. T., May 1964.

D. T. Llewellyn-Jones

References

1. S. C. Brown, G. Bekefi, and R. E. Whitney, J. Opt. Soc. Am. 53, 448 (1963).

2. H. A. Gebbie, Symposium on Interferometry, Teddington, England, 1959.

3. J. Strong and G. A. Vanesse, J. Opt. Soc. Am. 49, 844 (1959).

4. P. Fellgett, J. phys. radium 19, 187; 237 (1958).

5. R. C. Jennison, Fourier Transforms and Convolutions for the Experimentalist (Pergamon Press, London, 1963), Chapter V.

6. P. L. Richards, Far-Infrared Symposium, Riverside California, 1964 (sponsored by Naval Ordnance Laboratory, Corona, California).

E. THREE-DIMENSIONAL PLASMA DIFFUSION

The transport of plasma in a magnetic field occurs either quiescently by normal diffusion processes or in a turbulent fashion by macroscopic instabilities. The turbulent plasma always results in an excessive or enhanced loss of particles to the walls; whereas the quiescent plasma may have an enhanced or diminished loss to the walls. The latter effect has been demonstrated both theoretically and experimentally[1] for axisymmetric geometry with two degrees of freedom, radially across the field, and axially along the field. In the more general problem of three-dimensional diffusion in a rectangular cavity, it is of interest to determine all possible currents and the boundary conditions for achieving them.

In this analysis we invoke the usual condition of plasma neutrality, $n = n_+ = n_-$, but

there is no assumption about the currents. We start with the continuity and flow equations for the electrons and ions, and complete the set with Maxwell's equation for a conservative electric field, $\overline{\nabla} \times \overline{E} = 0$. The number of equations is sufficient to solve for the variables, but we choose to eliminate $\overline{E}$ from the set. So doing, we obtain a complete set of seven equations for the seven unknowns, $\overline{\Gamma}_+$, $\overline{\Gamma}_-$, and n.

$$\nabla_x \Gamma_{+x} + \nabla_y \Gamma_{+y} + \nabla_z \Gamma_{+z} = n\nu_i \tag{1}$$

$$\nabla_x \Gamma_{-x} + \nabla_y \Gamma_{-y} + \nabla_z \Gamma_{-z} = n\nu_i \tag{2}$$

$$\frac{\Gamma_{+x}}{\mu_+} + \frac{\Gamma_{-x}}{\mu_-} = -T\nabla_x n + B(\Gamma_{+y} - \Gamma_{-y}) \tag{3}$$

$$\frac{\Gamma_{+y}}{\mu_+} + \frac{\Gamma_{-y}}{\mu_-} = -T\nabla_y n + B(\Gamma_{-x} - \Gamma_{+x}) \tag{4}$$

$$\frac{\Gamma_{+z}}{\mu_+} + \frac{\Gamma_{-z}}{\mu_-} = -T\nabla_z n \tag{5}$$

$$\nabla_y \left(\frac{\Gamma_{+x} - \mu_+ B\Gamma_{+y}}{n} \right) = \nabla_x \left(\frac{\Gamma_{+y} + \mu_+ B\Gamma_{+x}}{n} \right) \tag{6}$$

$$\nabla_z \left(\frac{\Gamma_{+x} - \mu_+ B\Gamma_{+y}}{n} \right) = \nabla_x \left(\frac{\Gamma_{+z}}{n} \right). \tag{7}$$

Equations 1 and 2 are continuity, Eqs. 3, 4, and 5 are obtained by eliminating the components of $\overline{E}$ from pairs of ion and electron flow equations, and Eqs. 6 and 7 are obtained from the components of the ion flow equation by using $\overline{\nabla} \times \overline{E} = 0$. The corresponding electron equations are redundant, since they can also be obtained by substituting (3) and (4) in (6) and (7).

This technique of eliminating $\overline{E}$ has greatly simplified the problem, and five linear equations and two nonlinear equations, (6) and (7), result. It is possible at this point to assume the fundamental mode for the density and solve for the currents and characteristic value of ν_i. If this is the case, however, it should be proved rather than assumed. In the previous analysis,[1] it was shown that for two-dimensional diffusion, the uniqueness of the fundamental mode was consistent with $\overline{\nabla} \times \overline{E} = 0$. Similar constraints will be placed on the three-dimensional case which it has not yet been possible to show. It is possible to analyze the other two-dimensional case with both dimensions perpendicular to B, that is, x and y. Thus assuming uniformity in z, we eliminate Eqs. 5 and 7 and end up with one nonlinear and four linear equations. From the linear subset, one can Fourier-analyze the density and solve for the currents. Using the nonlinear equation (Eq. 6) for the total solution, one can show that the higher modes are not permissible.

The final result is

$$\nu_i = b_a D_a(\alpha^2+\beta^2) \tag{8}$$

with

$$\alpha = \pi/L_x$$

$$\beta = \pi/L_y$$

$$b_a = \left(1+\mu_+\mu_-B^2\right)^{-1},$$

and

$$\Gamma_{\pm x} = \alpha b_a D_a \sin \alpha x \cos \beta y \pm \mu_\pm B\beta b_a D_a \cos \alpha x \sin \beta y \tag{9}$$

$$\Gamma_{\pm y} = \beta b_a D_a \cos \alpha x \sin \beta y \mp \mu_\pm B\alpha b_a D_a \sin \alpha x \cos \beta y. \tag{10}$$

Having obtained this particular solution, we now look for a homogeneous solution for the currents that might flow as a result of asymmetric potentials applied to the walls. It has not been possible to find any additional solutions, and the conclusion is that (9) and (10) are complete. It is possible to test this conclusion experimentally, and the equipment is now being assembled.

D. R. Whitehouse

References

1. D. R. Whitehouse and H. B. Wollman, Plasma diffusion in a magnetic field, Phys. Fluids 6, 1470 (1963).

F. RADIOFREQUENCY RESONANCE PROBE

Takayama, Ikegami, and Miyazaki[1] have shown experimentally that an RF voltage applied to a Langmuir probe immersed in a plasma produces a resonance in the DC electron current at a frequency ω near (but below) the plasma frequency $\omega_p = Ne^2/m\epsilon_o$. More recently[2] a similar resonance, together with an antiresonance at a somewhat higher frequency, has been observed in the RF current picked up by a coil wound around the lead energizing the probe. The theory for this phenomenon, proposed by Harp,[3] indicates that the effect is primarily due to a sheath resonance and that the frequency of the resonance depends on the probe size and shape and on the thickness of the sheath. This note concerns the measurement and theory for a geometry most easily amenable to theoretical interpretation, namely that of a dipole probe.

The apparatus (Fig. X-17) consists of a circular metal ground plate that acts as the

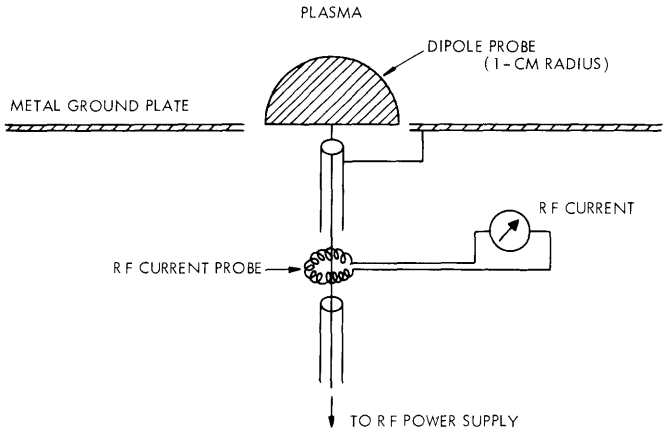

Fig. X-17. Schematic diagram of the experiment.

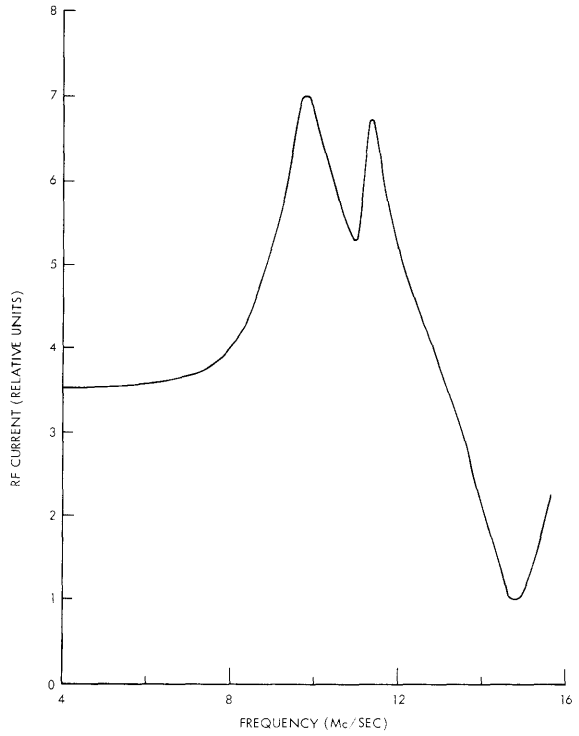

Fig. X-18. Magnitude of the RF probe current as a function of frequency ($\gamma/\omega_p \approx 0.1$).

image plane for the hemispherical RF probe. A tenuous plasma is formed above the plate by shooting low-energy electrons into un-ionized argon gas maintained at a pressure between 10^{-4} torr and 5×10^{-3} torr.

A measurement of RF current versus frequency is shown in Fig. X-18. We see a resonance in RF current that is typically of the form of a double peak and has the character of a dispersion curve (at higher pressure this dispersion character disappears presumably because electron-atom collsions broaden out the resonance). We also observe a sharp "antiresonance" at a somewhat higher frequency. These measurements agree with earlier observations.[2]

1. Theory

Consider a general plasma system completely enclosed by a perfectly conducting enclosure coupled to a waveguide (Fig. X-19). According to Bers,[4] the (complex) susceptance B at a reference plane in the waveguide of Fig. X-19, defined as

$$I = jBV,$$

is given by

$$B|V|^2 = \omega\epsilon_o \int |E|^2 K \, dV, \tag{1}$$

where I and V are the equivalent RF current and voltage at the reference plane, K is the dielectric coefficient of the medium at any point within the enclosure, and E is the

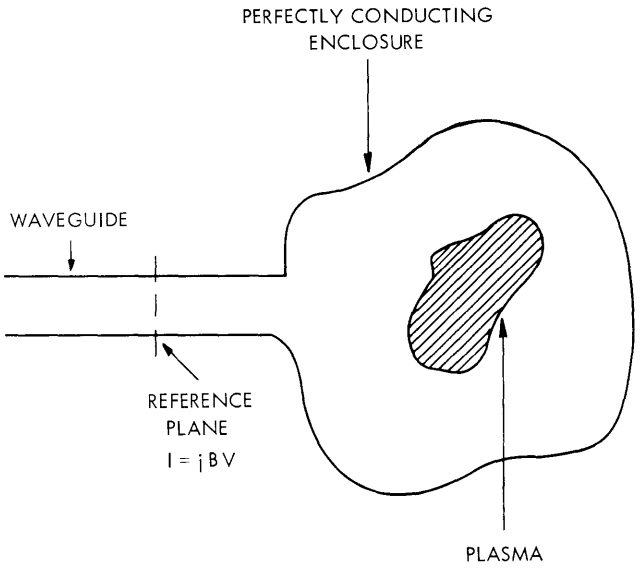

Fig. X-19. Plasma system coupled to a waveguide.

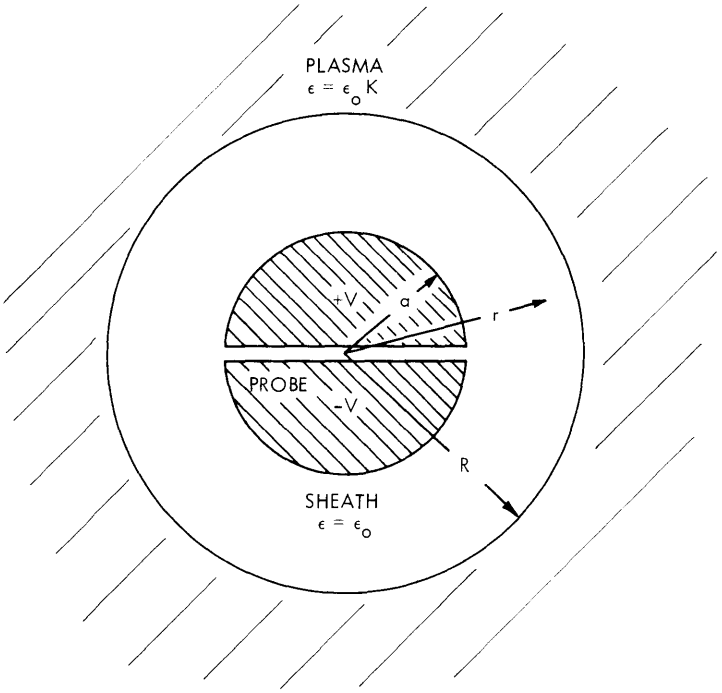

Fig. X-20. Simplified model of the RF probe.

electric field; the integration in Eq. 1 extends over the enclosure volume. Contributions from the magnetic field to the right-hand side of Eq. 1 are neglected, since H = 0 in the low-frequency, quasi-static approximation that is to be used. (Note also that the conducting walls of the enclosure can be removed to infinity, provided the fields fall off sufficiently quickly with distance.)

The problem is to calculate the susceptance B for the plasma system of Fig. X-17. The simplified model is shown in Fig, X-20. An alternating RF voltage is applied to the spherical probe of radius a. The probe is surrounded by a sheath of radius R; the sheath is taken to be an empty cavity, and the presence of electrons is neglected (as was also assumed by Harp). Beyond the sheath (r > R) the plasma is taken to be uniform; its dielectric coefficient, in the quasi-static approximation (wavelength $\lambda \to \infty$), is

$$K = 1 - \frac{\omega_p^2/\omega}{\omega - j\gamma}, \tag{2}$$

where γ is the electron-atom collision frequency. Landau damping of the longitudinal oscillations is neglected. This is not a bad approximation for frequencies $\omega < 0.8\omega_p$, as Pavkovich and Kino[5] showed.

The solution for B then reduces to a simple electrostatic problem with potentials ϕ of the form

$$\phi = \sum_{\ell=0}^{\infty} \left[A_\ell r^\ell + B_\ell r^{-(\ell+1)}\right] P_\ell(\cos\theta); \qquad R \geq r \geq a$$

$$= \sum_{\ell=0}^{\infty} C_\ell r^{-(\ell+1)} P_\ell(\cos\theta); \qquad r \geq R$$

and boundary conditions

$$\left.\begin{aligned} \phi(\theta) &= +V \quad \text{for } 0 \leq \theta \leq \frac{\pi}{2} \\ &-V \quad \text{for } \frac{\pi}{2} < \theta \leq \pi \end{aligned}\right\} \qquad \text{at } r = a$$

$$\left.\begin{aligned} -\epsilon_o \frac{\partial\phi(r\leq R)}{\partial r} &= -\epsilon \frac{\partial\phi(r\geq R)}{\partial r} \\ -\frac{1}{R}\frac{\partial\phi(r\leq R)}{\partial\theta} &= -\frac{1}{R}\frac{\partial\phi(r\geq R)}{\partial\theta} \end{aligned}\right\} \qquad \text{at } r = R.$$

The final result for the susceptance B is a sum of contributions from all odd multipoles ($\ell = 1, 3, 5 \ldots$) and is given by

$$\frac{B}{4\pi\epsilon_o \omega a} = \sum_{\ell=0}^{\infty} \frac{D_\ell^2}{(2\ell+1)^2} \left\{ [\ell^2 + \ell(\ell+1)]\, a_\ell^2 \left[f^{2\ell+1} - 1\right] + [(\ell+1)^2 + \ell(\ell+1)] \left[\beta_\ell^2 \left[1 - \frac{1}{f^{2\ell+1}}\right] + K\gamma_\ell^2 \frac{1}{f^{2\ell+1}}\right]\right\} \tag{3}$$

where

$$a_\ell = \left(1 - \frac{1}{Q_\ell}\right); \qquad f = R/a$$

$$\beta_\ell = \frac{1}{Q_\ell}$$

$$\gamma_\ell = \left[\frac{1}{Q_\ell} + \left(1 - \frac{1}{Q_\ell}\right) f^{2\ell+1}\right]$$

$$Q_\ell = 1 + \frac{(\ell+1)(1-K)}{\ell + K(\ell+1)} \frac{1}{f^{2\ell+1}}$$

$$D_\ell = (2\ell+1)\left[\frac{(-1)(-3)\ldots(-\ell+2)}{(\ell+1)(\ell-1)\ldots 2}\right] \qquad \text{for } \ell = 1,3,5\ldots$$

$$= 0 \qquad \text{for } \ell = 0,2,4,6\ldots .$$

Equation 3 has not yet been evaluated in detail. When one neglects collisional damping ($\gamma \equiv 0$ and thus K is purely real) and assumes (probably incorrectly) that the dominant contribution to B comes from the dipole term $\ell = 1$ only, then B plotted as a function

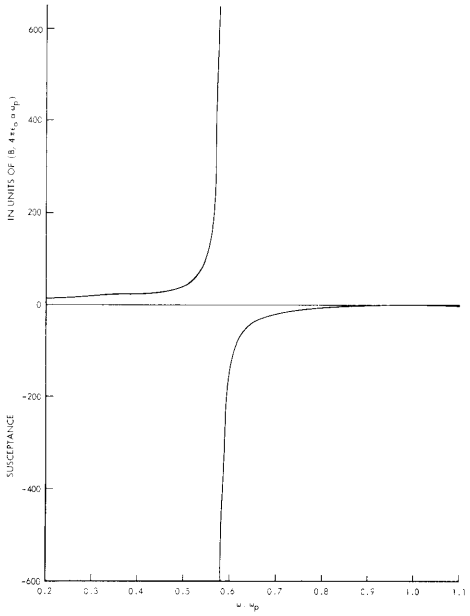

Fig. X-21. Susceptance as a function of frequency for the dipole mode ($\ell = 1$) and zero collisions ($\gamma = 0$). $f = 2^{1/3}$.

of ω is of the form shown in Fig. X-21. We note a dispersionlike resonance together with an "antiresonance" when B becomes zero. The resonance occurs at a frequency given by

$$\frac{\omega}{\omega_p} = \sqrt{\frac{2}{3}}\sqrt{\frac{f^3-1}{f^3}} \qquad \text{as } B \to \infty \tag{4}$$

and the antiresonance at

$$\frac{\omega}{\omega_p} = \sqrt{\frac{2f^3+1}{3f^3}} \qquad \text{as } B \to 0 \tag{5}$$

In contrast, Harp predicts a resonance at

$$\frac{\omega}{\omega_p} = \sqrt{\frac{f-1}{f}} \qquad \text{as } B \to \infty \tag{6}$$

and an antiresonance at

$$\frac{\omega}{\omega_p} = 1 \qquad \text{as } B \to 0. \tag{7}$$

This disagreement comes from Harp's assumption of an isotropic spherically symmetric excitation of the probe (i.e., ϕ is given by the monopole value $\ell = 0$). This mode is not excited in our geometry, and it is unlikely that it is excited in the measurements of several of the previous workers.

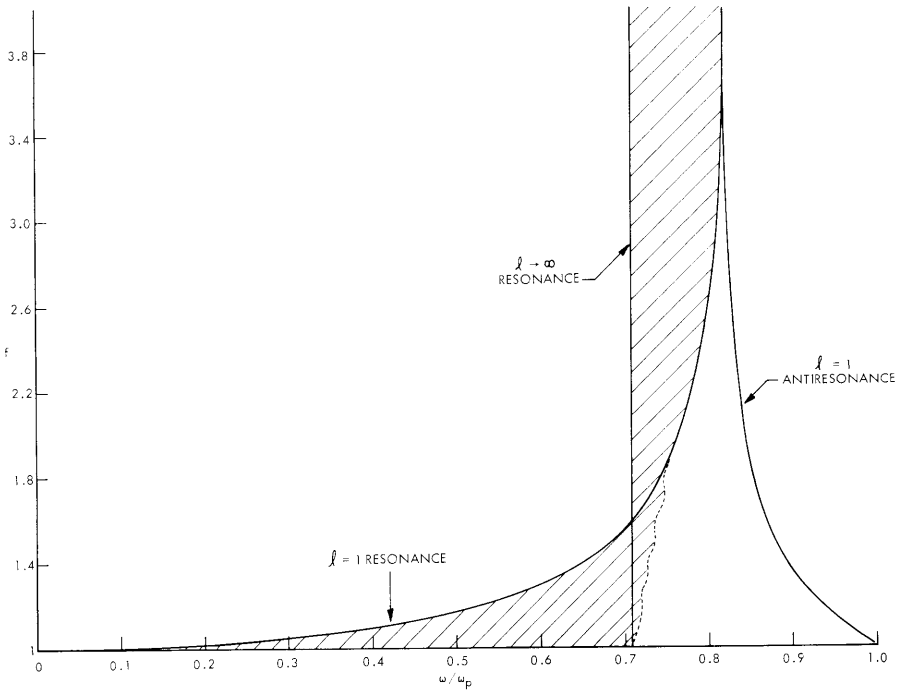

Fig. X-22. Location of the dipole resonance $\ell = 1$, $B \to \infty$, the multipole resonance $\ell \to \infty$, $B \to \infty$, and the "antiresonance" $\ell = 1$, $B \to 0$, as a function of the probe size $f = R/a$. The shaded region shows location of all multipole resonances higher than $\ell = 1$.

Figure X-22 shows how the frequencies at resonance and antiresonance vary with $f \equiv R/a$. The figure also shows the position of the resonance for the multipole $\ell \to \infty$. All resonances belonging to higher order multipoles in the range $\ell = 1\text{-}\ell \to \infty$ lie within the shaded region of the figure. Since all resonances are well removed from $\omega = \omega_p$, Landau damping can be safely neglected in the calculations, even for infinitesimally small probes $f \to \infty$. This conclusion differs from Harp's who on the basis of the monopole calculation (Eq. 6, $\omega/\omega_p \to 1$ as $f \to \infty$) deduces that the resonances of small probes vanish as a result of Landau damping.[5]

Assuming that in the experiment illustrated in Fig. X-18 only the dipole resonance

was excited and not the higher odd multipoles, we can, by a simultaneous solution of Eqs. 4 and 5, deduce ω_p and f. Taking $(\omega)_{resonance} = 10.5$ mc and $(\omega)_{antiresonance} = 14.8$ mc, f = 1.36. Then the sheath thickness $t = a(f-1) = 0.36a$. With the measured value of electron temperature set equal to 2.2 ev, t becomes approximately 2 Debye lengths. This differs significantly from the value $t = 5\lambda_D$ that was assumed by Harp on the basis of an extrapolation made from theory[6] for an infinite plane metal sheet in contact with the plasma. Indeed, comparison with other measurements made by us and previous workers[2] suggests that t is a rather strong function of probe size. To use the resonance probe for diagnostic purposes it is, therefore, necessary to obtain an experimental or theoretical relationship between t, a, and λ_D. Electron temperature and density could be then determined. Also, a calculation of the resonance linewidth can be used in a determination of the collision frequency γ.

D. F. Smith, G. Bekefi

References

1. K. Takayama, H. Ikegami, and S. Miyazaki, Phys. Rev. Letters 5, 238 (1960); H. Ikegami and K. Takayama, Report IPPJ-10, Institute of Plasma Physics, Nagoya University, 1963.

2. J. Uramoto, J. Fujita, H. Ikegami, Report IPPJ-19, Institute of Plasma Physics, Nagoya University, 1963.

3. R. S. Harp, Microwave Research Laboratories, Stanford University, Stanford, California (unpublished report).

4. W. P. Allis, S. J. Buchsbaum, and A. Bers, Waves in Anisotropic Plasmas, (The M. I. T. Press, Cambridge, Mass., 1963), pp. 101-102.

5. The antiresonances, however, are much closer to $\omega = \omega_p$ than the resonances, and here Landau damping may play a major role. If this is indeed the case, the position of the antiresonances is expected to be at $\omega = \omega_p$ rather than at the value given by Eq. 5.

6. J. Pavkovich and G. S. Kino, Report No. 1077, Microwave Research Laboratory, Stanford University, Stanford, California, 1963.

G. FAST-WAVE RELATIVISTIC AND RADIATION-PRESSURE AMPLIFICATION MECHANISMS

Amplification of electromagnetic radiation in an electron gas in the fast-wave interaction mode near electron-cyclotron resonance has been predicted by many authors.[1-4] Several different mechanisms exist. One mechanism, which has been labeled the relativistic mechanism, can also operate at nonrelativistic electron energies. It depends on the variation of $\omega_b - \omega$ with $(v/c)^2$ at cyclotron resonance. The term ω_b is the electron-cyclotron frequency in radians per second.

$$\omega_b = \frac{|e|}{m_o} B\left[1 - \left(\frac{v}{c}\right)^2\right]^{1/2} \equiv \omega_{bo}\left[1 - \left(\frac{v}{c}\right)^2\right]^{1/2}. \tag{1}$$

The term ω is the electromagnetic wave frequency in radians per second, experienced in a coordinate system moving with the guiding center of the electron.

$$\omega = \omega_o\left[1 \pm \frac{v_z}{v_p}\right]. \tag{2}$$

The term (v/c) is the ratio of electron speed to the speed of light, and v_z/v_p is the ratio of the electron speed in the direction of the external magnetic field to the phase velocity of the electromagnetic wave in the direction of the external magnetic field.

$$v_p = \frac{c}{\cos\theta}.$$

The propagation vector of the electromagnetic wave is inclined at an angle θ to the external magnetic field. The magnitude of the magnetic induction of the external magnetic field is B. The ratio of the charge to rest mass of the electron is e/m_o. The electromagnetic wave frequency, in radians per second, is ω_o in the rest frame. A second mechanism, which we label the radiation-pressure mechanism can also lead to gain. This mechanism depends on the variation of $\omega_b - \omega$ with v_z/v_p at cyclotron resonance. There are other mechanisms that will not be considered in this report.

The predictions of these gain mechanisms by Twiss[1] and by Bekefi, Hirshfield, and Brown[2] were deduced from macroscopic considerations of the transport of radiation through plasmas. Schneider[3] presented a simple quantum-mechanical model of the relativistic mechanism. Chow and Pantell[4] presented a mixture of microscopic and macroscopic arguments to discuss the radiation-pressure mechanism. We present here the simple classical macroscopic (particle) picture of both mechanisms. This model displays essential characteristics of the two mechanisms:

(i) Conditions for amplification.

(ii) Demarcation of the region of reduction of the absorption coefficient, or amplification from the region of enhanced absorption, as functions of ω_{bo}/ω_o.

The explanation of these mechanisms is based on the following line of reasoning.

1. An electron gas in the absence of a velocity dependence of $\omega_b - \omega$ absorbs energy from the electromagnetic wave. This absorption occurs because the primary force between the electron and wave is $e\underline{v_T} \cdot \underline{E_1}$. Because v_T increases for the absorbing electron and decreases for the emitting electron, the interaction, $\underline{v_T} \cdot \underline{E_1}$, increases for absorbing electrons and decreases for emitting electrons, with the result that there is net absorption in any time interval, provided that the electrons are initially uniformly distributed in the emission and absorption phases.

2. The velocity dependence of $\omega_b - \omega$ leads to unequal flows of electrons from the

emission to absorption and from the absorption to emission phases. This leads to an unequivocal prediction of the regions of enhanced absorption and amplification as a function of ω_{b_o}/ω_o for each of the two mechanisms.

3. When the electron population in the emission phase exceeds that in the absorption phase by a certain value, the additional emission of the excess population overcomes the absorption expected from the increasing value of $\underline{v_T} \cdot \underline{E_1}$ in the absorption phase, and from the decreasing value of $\underline{v_T} \cdot \underline{E_1}$ in the emission phase.

4. Collisions, transit-time effects, and magnetic-field inhomogeneity tend to disrupt the flow of electrons from phase to phase. These effects determine an effective time of interaction (or the inverse, an effective collision frequency, ν, expressed in radians per second). This average time interval then determines: (a) the average emission phase population excess caused by the velocity dependence of $\omega_b - \omega$; (b) the average absorption resulting from the difference in $\underline{v_T} \cdot \underline{E_1}$ in the time interval $2\pi/\nu$ for absorbing and emitting electrons. Balance of these absorption and emission processes occurs at the onset of gain.

The electron gas is assumed to be uniform, monoenergetic, and infinite in extent. It has velocity components v_x, v_y, and v_z. The external magnetic field is in the z-direction and is uniform. The electromagnetic wave is a plane wave. The propagation vector is inclined at angle θ to the z-axis and lies in the xy plane. The electric vector points in the direction of the x-axis. The subscript 1 refers to the electromagnetic wave. The three components of the Lorentz equation are

$$m \frac{dv_x}{dt} = - |e| v_y B \left[1 + \frac{B_1}{B} \sin\theta \sin\omega t\right] + |e| v_z B_1 \cos\theta \sin\omega t - |e| E_1 \sin\omega t$$

$$m \frac{dv_y}{dt} = |e| v_x B \left[1 + \frac{B_1}{B} \sin\theta \sin\omega t\right]$$

$$m \frac{dv_z}{dt} = - |e| v_x B_1 \cos\theta \sin\omega t.$$

The electromagnetic forces are called weak when $E_1 \ll vB$. In this case, the first-order solution for v_x is

$$v_x = v_T \sin(\omega_b t + \phi_o),$$

where v_T and ω_b are slowly varying functions of time. Appreciable variations in v_T and ω_b occur only in times that are long compared with $2\pi/\omega_b$. $v_T^2 = \overline{v_x^2 + v_y^2}$. The term v_T is the speed of the electron transverse to the external magnetic field.

The ratio of the longitudinal and transverse forces (with respect to the direction of the external magnetic field) between the electron and electromagnetic wave is

$$\frac{m\, dv_z/dt}{m\, dv_T/dt} \approx \frac{v_T B_1 \cos\theta}{E_1} = \frac{v_T}{v_p}.$$

The ratio of the kinetic energy change of the longitudinal and transverse components of motion is

$$\frac{mv_z\, dv_z/dt}{mv_T\, dv_T/dt} = \frac{v_z}{v_p}.$$

Therefore, for nonrelativistic electrons, we may take the kinetic-energy change of the electrons as the change in the transverse component:

$$\frac{1}{2} m \frac{dv^2}{dt} \approx mv_T \frac{dv_T}{dt}.$$

Then,

$$mv_T \frac{dv_T}{dt} = \underline{F} \cdot \underline{v} \approx - |e| E_1 v_T \sin(\omega_b t + \phi_o) \sin \omega t,$$

or

$$\frac{dv_T}{dt} = - \frac{2|e|}{m} E_1 \sin(\omega_b t + \phi_o) \sin \omega t. \tag{3}$$

The term ϕ_o is the initial phase angle, with respect to time, between v_x and E_1.

When ω_b and ω are not velocity dependent (3) has the familiar solution

$$v_T = v_{T_o} - \frac{|e|}{m} E_1 \left[\sin\phi_o \frac{\cos(\omega-\omega_b)t - 1}{\omega - \omega_b} - \cos\phi_o \frac{\sin(\omega-\omega_b)t}{\omega - \omega_b} \right]. \tag{4}$$

The kinetic energy as a function of time for each electron is found by squaring (4). It is assumed that initially the electrons are uniformly distributed over all phases, ϕ_o. The average kinetic-energy density change of the electron gas in the time $2\pi/\nu$ is found by multiplying the square of (4) by $\frac{1}{2}m$, integrating over all phases, and normalizing the answer by dividing by $2\pi/n$, where n is the electron density. This gives

$$\Delta k = \frac{\epsilon_o E_1^2}{2} \frac{\omega_p^2}{\nu^2} \left[4\pi^2 \frac{1 - \cos\chi}{\chi^2} \right] \text{joules/meter}^3,$$

where $\chi = \frac{2\pi}{\nu}(\omega-\omega_b)$, and $\omega_p^2 = \frac{ne^2}{\epsilon_o m}$.

The power absorption per unit volume is

$$P = \frac{\epsilon_o E_1^2}{2} \frac{\omega_p^2}{\nu} \left[2\pi \frac{1 - \cos \chi}{\chi^2} \right] \text{watts/meter}^3. \tag{5a}$$

The maximum power absorption per unit volume, occurs at cyclotron resonance and is

$$P_M = \pi \frac{\epsilon_o E_1^2}{2} \frac{\omega_p^2}{\nu} \text{ watts/meter}^3. \tag{5b}$$

The emission by the average excess population of the emission phase must exceed P for gain to occur.

1. Excess Phase Population by the Relativistic Mechanism

The rate of change of phase of the electron transverse velocity vector with respect to the electric field of the wave is

$$\frac{d\phi}{dt} = \omega_b - \omega. \tag{6a}$$

In the case of the relativistic mechanism Eq. 1 for ω_b is substituted in (6a). When $v/c \ll 1$, we have

$$\begin{aligned} \frac{d\phi}{dt} &\approx \omega_{b_o} \left[1 - \frac{1}{2} \left(\frac{v}{c} \right)^2 \right] - \omega \\ &= \omega_{b_o} \left[\left(1 - \frac{\omega}{\omega_{b_o}} \right) - \frac{1}{2} \left(\frac{v}{c} \right)^2 \right]. \end{aligned} \tag{6b}$$

Two regions can be considered

(a) $\frac{\omega}{\omega_{b_o}} < 1 - \frac{1}{2} \left(\frac{v}{c} \right)^2$

(b) $\frac{\omega}{\omega_{b_o}} > 1 - \frac{1}{2} \left(\frac{v}{c} \right)^2$.

In region (a) $d\phi/dt$ is positive; $d\phi/dt$ decreases for absorbing electrons and increases for emitting electrons. Thus, in this region, a population excess will build up in the absorption phase and only enhanced absorption can be expected. In region (b) $d\phi/dt$ is negative. The magnitude of $d\phi/dt$ increases for absorbing electrons and decreases for emitting electrons. In this region the population excess builds up in the emission phase and amplification is possible. The expression for v_T as a function of time with the replacement of v_{T_o} by $v_o = \left(v_{T_o}^2 + v_z^2 \right)^{1/2}$ in (4) is substituted in (6b). Equation 6b

is then integrated with respect to time. This gives the change in phase, as a function of time, of an electron of initial phase ϕ_o. The resulting expression is integrated over all ϕ_o in each phase and the difference yields the net phase change, $\Delta\phi$. Since the electrons were initially distributed uniformly over all phases with a phase density $n/2\pi$ electrons per radian per unit volume, the excess population becomes $\Delta n \approx n\,\Delta\phi/2\pi$ electrons per unit volume. The resulting expression for Δn, after carrying out the indicated integrations, is

$$\Delta n = 4n \frac{|e|}{m} \frac{\omega_{b_o} v_{T_o} E_1}{c^2 \nu^2} \frac{1 - \cos\chi}{\chi^2}.$$

When (4) is squared, the first-order term for the kinetic energy change of an electron of initial phase ϕ_o is

$$\Delta k = v_{T_o} |e| E_1 \left[\sin\phi_o \frac{\cos(\omega-\omega_b)t}{\omega - \omega_b} - \cos\phi_o \frac{\sin(\omega-\omega_b)t}{\omega - \omega_b} \right].$$

This is averaged over the entire emission phase to yield

$$\overline{|\Delta k|} = v_{T_o} |e| E_1 \frac{\sin(\omega-\omega_b)t}{\pi(\omega-\omega_b)}$$

$$= \frac{2 v_{T_o} |e| E_1}{\nu^2} \frac{\sin\chi}{\chi}.$$

Thus the gain condition to first order is $\Delta n \overline{|\Delta k|} > \overline{P}$, which yields

$$\left(\frac{v_{T_o}}{c}\right)^2 > \frac{\pi^2}{8} \frac{\nu}{\omega_{b_o}} \frac{\chi}{\sin\chi} \approx \frac{\nu}{\omega_{b_o}} \frac{\chi}{\sin\chi},$$

when

$$\omega_{b_o} < \omega - \frac{1}{2}\left(\frac{v}{c}\right)^2.$$

One necessary condition for the validity of this analysis is that $\Delta n/n \ll 1$. At the onset of gain $\left(v_{T_o}/c\right)^2 \sim \nu/\omega_{b_o}$ and

$$\frac{\Delta n}{n} \sim \frac{E_1}{v_{T_o} B} \left(\frac{c}{v_{T_o}}\right)^2.$$

When $E_1 = 10^2$ volt/meter, $B = 0.3$ weber/meter^2, and $v_{T_o} \approx 10^7$ meter/second,

$$\frac{\Delta n}{n} \sim 0.03.$$

2. Excess Phase Population by the Radiation Pressure Mechanism

In this case Eq. 6 is written

$$\frac{d\phi}{dt} = \omega_b - \omega_o(1 \mp v_z/v_p).$$

The minus and plus signs refer to the forward and backward wave interaction modes, respectively. Consider the forward wave, $\omega = \omega_o(1-v_z/v_p)$. If $\omega_b > \omega$, initially, then $d\phi/dt > 0$. An electron in an absorbing phase experiences a force in the direction of $+v_z$, according to $\underline{F_z} = -|e|\underline{v_T} \times \underline{B_1}$. Therefore, for this electron dv_z/dt is positive. The result is a mechanism for building an excess population in the emitting phase, since $|d\phi/dt|$ increases, that is,

$$\frac{d^2\phi}{dt^2} = \frac{\omega_o}{v_p}\frac{dv_z}{dt}.$$

Electrons in an emitting phase experience a force in the direction of $-v_z$, and $|d\phi/dt|$ decreases. Next consider the backward wave, $\omega = \omega_o(1+v_z/v_p)$. Here

$$\frac{d^2\phi}{dt^2} = -\frac{\omega_o}{v_p}\frac{dv_z}{dt}.$$

In this case, an electron in the absorbing phase experiences a deceleration in the direction of v_z, and $d^2\phi/dt^2 > 0$. Thus again if $\omega_b > \omega$, there is a mechanism for producing an excess population in the emission phase. Again, consider the forward-wave interaction. From the z component of the Lorentz equation,

$$\frac{dv_z}{dt} = -\frac{|e|}{m} v_x B_1 \cos\theta \sin\omega t.$$

Substituting $v_x = v_T \sin(\omega_b t + \phi_o)$, we obtain

$$\frac{dv_z}{dt} = -\frac{|e|}{m}\frac{v_T}{2} B_1 \cos\theta [\cos\phi_o \cos(\omega_b - \omega)t - \sin\phi_o \sin(\omega_b - \omega)t].$$

A first-order solution for v_z is obtained by integration of the expression above, the small-time variations of v_T and ω being neglected:

$$v_z = v_{z_o} - \frac{|e|}{m}\frac{v_T}{2} B_1 \cos\theta \left[\cos\phi_o \frac{\sin(\omega_b-\omega)t}{\omega_b-\omega} + \sin\phi_o \frac{\cos(\omega_b-\omega)t - 1}{\omega_b-\omega}\right].$$

Then, using $B_1 = E_1/c$, we obtain

$$\frac{d\phi}{dt} = \left(\omega_b - \omega_o - \frac{v_{z_o}}{v_p}\right) + \frac{1}{2}\frac{|e|}{m}\frac{v_T\omega_o E_1}{v_p^2}\left[\cos\phi_o \frac{\sin(\omega_b-\omega)t}{\omega_b-\omega} + \sin\phi_o \frac{\cos(\omega_b-\omega)t - 1}{\omega_b-\omega}\right].$$

This expression is averaged over the absorption phase and the emission phases separately, and the difference is integrated with respect to time and multiplied by $n/2\pi$ to obtain the population excess. The result is

$$\Delta n = n\frac{\omega_o}{\nu^2}\frac{|e|}{m}\frac{v_T}{v_p^2} E_1 \left[2\frac{\cos\chi - 1}{\chi^2}\right].$$

The onset of gain condition is $\Delta n|\overline{\Delta k}| > \overline{P}$, which yields

$$\left(\frac{v_T}{v_p}\right)^2 > \frac{\pi^2}{4}\frac{\nu}{\omega_o}\frac{\chi}{\sin\chi}.$$

J. D. Coccoli

References

1. R. Q. Twiss, Australian J. Phys. 11, 564 (1958).

2. G. Bekefi, J. L. Hirschfield, and S. C. Brown, Phys. Fluids 4, 173 (1961).

3. J. Schneider, Phys. Rev. Letters 2, 504 (1959).

4. K. K. Chow and R. H. Pantell, A Small Signal Analysis of the Electron Cyclotron Backward-Wave Oscillator, Microwave Laboratory Report 851, Stanford University, Stanford, California, October 1961.

H. MEASUREMENT OF NEUTRAL-GAS TEMPERATURE IN A PLASMA COLUMN*

Ordinarily, in a glow discharge the temperature of the neutral-gas component in the discharge is of little importance, and no particular attention seems to have been given to the problem of measuring this quantity. In experiments dealing, for example, with the influence of gas flow on the properties of the discharge, the neutral-gas temperature does play a significant role because for a given mass flow the flow velocity in the discharge region is directly proportional to the temperature. In the present study, dealing

*This work was supported in part by the U. S. Navy (Office of Naval Research) under Contract Nonr-1841(42).

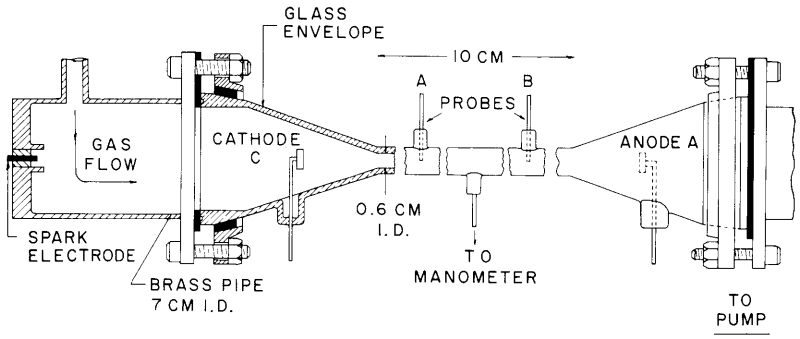

Fig. X-23. Experimental arrangement.

with an argon discharge, the gas temperature in the plasma column of the discharge is determined from measurements of the speed of sound in the column. These measurements have shown that a Langmuir probe can be used as an acoustic detector.

The acoustic signal used in these experiments is a pulse produced by discharging capacitors into a spark gap located in the neutral gas outside the plasma column of the discharge as indicated in Fig. X-23, where the over-all experimental apparatus is shown. The current pulse in the discharge lasts approximately 60 μsec with a peak current of 1500 amps. Delivered into argon, the voltage across the gap is almost constant at 20 volts, just a few volts above the first ionization potential. The total energy supplied is approximately 1 joule.

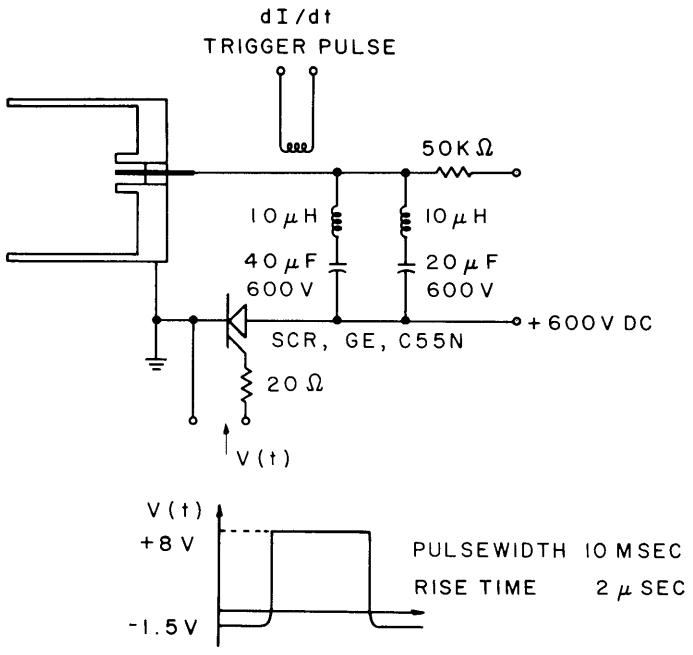

Fig. X-24. Spark generator.

Switching the capacitors with a silicon-controlled rectifier (SCR) obviates the need for high-voltage triggered spark-gap equipment, which would otherwise be required for rapid switching of high currents. The circuit modifications necessary for use of an SCR in high-current applications are all simple (see Fig. X-24). The air inductors in series with the capacitors are chosen to limit the initial and peak values of current to the appropriate rated values of the SCR. The shape of the triggering pulse is chosen to keep the SCR safely off until triggered, but then to turn it on fully and quickly for the high-current surge. The capacitor bank must not be recharged until the triggering pulse has returned to negative bias.

The method of using Langmuir probes as acoustic detectors is based on the observation of the ion density fluctuations produced by the sound wave. If one considers the ions and the neutral gas as moving together, the relative density fluctuations in the neutral gas and in the ion gas should be approximately the same, the electric fluctuating forces being considerably smaller than the pressure forces. The ion density fluctuations are detected as fluctuations in the current drawn by a Langmuir probe biased to collect all ions entering its sheath.

The bias voltage V_s is set a few volts below the voltage that is measured with the probe when connected only to a high-impedance voltmeter. V_s can be supplied by the network shown in Fig. X-25 with low internal impedance for high-frequency changes in load so that V_s remains a pure fixed DC level to ground. If these conditions are met,

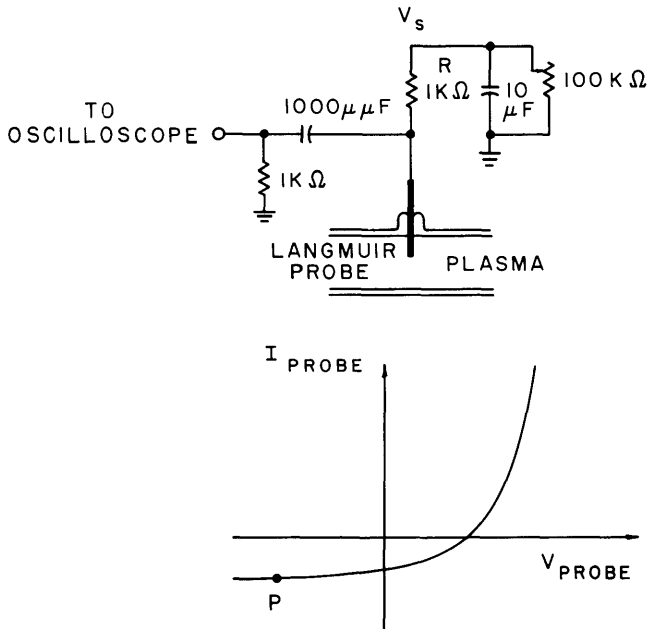

Fig. X-25. Probe circuit.

then the fluctuations in probe voltage are caused by changes in the current through the resistor R; they represent changes in the probe current. There is, however, considerable noise and low-frequency oscillation in the plasma, and it is desirable to discriminate against it. This can be done by differentiating the signal with the simple RC network shown, since the acoustic pulse to be detected has a fast-rising wave front and a larger derivative than the main part of the noise. Furthermore, the operating point P on the probe characteristic is chosen to lie on the nearly horizontal portion of the curve as shown in Fig. X-25 so that the current is approximately equal to the ion saturation current determined by the ion density at the probe. The current clearly is almost independent of the plasma probe potential V_b, and local oscillations in the plasma potential, representing the noise in the discharge, will cause only slight changes in the current. Thus, operating in this region of ion saturation of the probe and monitoring only the current, we discriminate against unwanted voltage fluctuations and obtain a signal proportional to the local ion density.

With the spark power of approximately 1 joule used in the experiments, the strength of the acoustic pulse traveling into the plasma was sufficient to produce an output signal from the Langmuir probe which was clearly noticeable above the noise on the probe. To measure the speed of sound in the plasma, it is convenient to record the difference in the output signals from two Langmuir probes separated a certain distance apart in the plasma as shown in Fig. X-23. A typical example of such an output signal from the two probes is shown in Fig. X-26. The marked changes in slope of the signal at points A and B indicate the passage of the acoustic pulse past the first and second probes, and the travel time between A and B is a direct measure of the speed of sound in the plasma.

From the measured speed, $c_m = \frac{\Delta \ell}{\Delta T}$, where $\Delta \ell$ is the separation between the probes and ΔT, the measured travel time of the acoustic pulse between the probes, we obtain the temperature in the following manner. If we denote the gas-flow velocity V, and the local speed of sound in the plasma column c, we have $c_m = c + V$. The volume rate Q_o

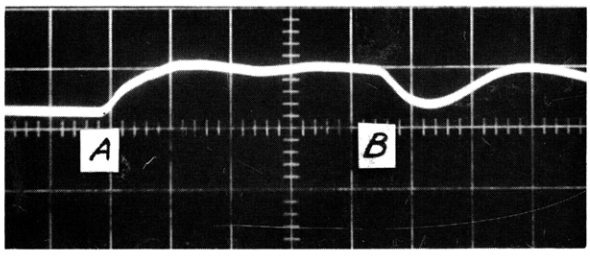

Fig. X-26. Typical output from the probe pair resulting from the passage of a sound pulse producing the discontinuities in slope at A and B. The separation between A and B represents the travel time of the pulse between the two probes.

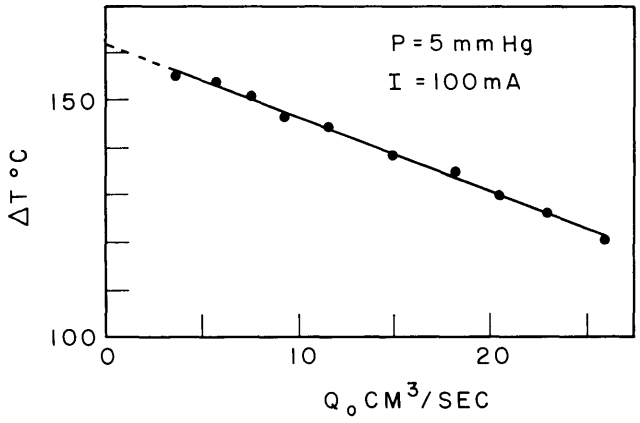

Fig. X-27. Measured neutral-gas temperature in the plasma column as a function of the gas-flow rate (referred to atmospheric pressure and room temperature) at a constant gas pressure of 5 mm Hg and discharge current 100 ma.

of the flow going through the plasma is measured at atmospheric pressure p_o and temperature T_o, and if the area of the discharge tube is A, the flow velocity is $V = \frac{\rho_o Q_o}{\rho A} = V_o \frac{T}{T_o}$, where T is the temperature in the plasma column, p the pressure, and $V_o = \frac{Q_o}{A_o} \frac{p_o}{p}$.

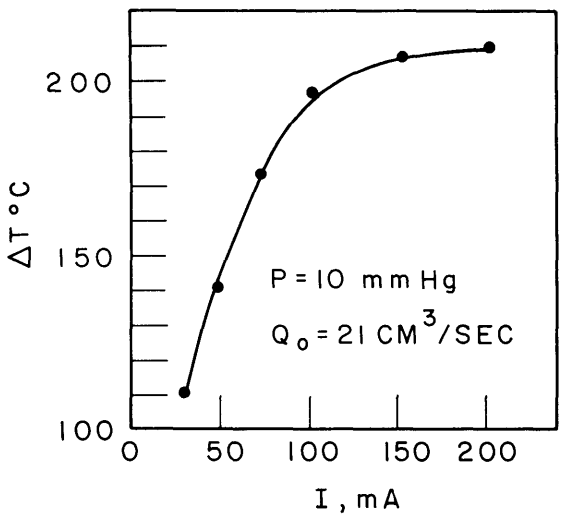

Fig. X-28. Typical dependence of gas temperature on the discharge current at constant pressure and gas flow.

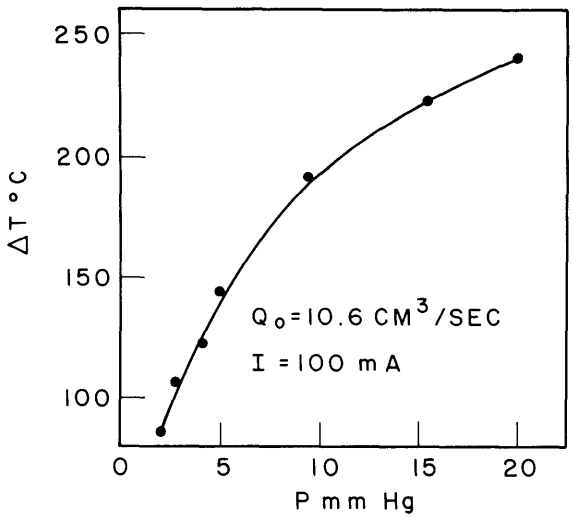

Fig. X-29. Typical dependence of gas temperature on gas pressure at constant discharge current and gas flow.

Similarly, if we denote the speed of sound at the ambient temperature T_o by c_o, the speed of sound in the plasma column is $c = \sqrt{T/T_o}$. The temperature T is then determined by

$$c_m = c + V = c_o\sqrt{T/T_o} + V_o \frac{T}{T_o}$$

from which follows

$$\sqrt{\frac{T}{T_o}} = \frac{1}{2m_o}\left[\sqrt{(1+2m_o)^2 + 4\frac{\Delta c}{c_o}m_o} - 1\right],$$

where $m_o = V_o/c_o$ and $\Delta c = c_m - (c_o+V_o)$. For sufficiently small values of $\Delta c/c_o$ we then obtain for $\Delta T = T - T_o$

$$\frac{\Delta T}{T_o} \approx \frac{\Delta c}{c_o}\frac{2}{(1+2m_o)}.$$

A typical curve showing the measured gas temperature as a function of the gas flow rate at a constant value of the gas pressure in the discharge is shown in Fig. X-27. An increase of the flow rate from zero to approximately 30 cc/sec (measured at atmospheric pressure and ambient temperature) results in an approximately linear decrease of the temperature from approximately 175°C to 120°C. Similar data have been obtained at several gas pressures in the range 5-20 mm Hg and for discharge currents between 40 ma and 200 ma. Typical curves showing the dependence of temperature on gas pressure and discharge current are given in Figs. X-28 and X-29.

K. W. Gentle, U. Ingard